**Title: Methane emissions intensity mapping from space reveals outsized emissions impact from marginal oil and gas production in the U.S.**

**Short title: Marginal oil/gas well-pads drive outsized methane emissions**


## Authors

James P. Williams[1], Joshua Benmergui[1,2], Mark Omara[1], Marvin Knapp[1,2], Anthony Himmelberger[3], Kaiya Weatherby[1], Ben Lyke[1], Katlyn MacKay[1], Jack Warren[1], Luis Guanter[1,4], Steven C. Wofsy[2], Steven P. Hamburg[1,3], Ritesh Gautam[1]

## Affiliations

[1]Environmental Defense Fund, New York, NY 10010, USA
[2]Harvard John A. Paulson School of Engineering and Applied Sciences, Cambridge, USA
[3]MethaneSAT, LLC, Austin, TX 78701, USA
[4]Research Institute of Water and Environmental Engineering (IIAMA), Universitat Politecnica de Valencia, Valencia, Spain



## Abstract

Methane emissions reduction from the oil/gas sector, the largest industrial methane source, is a widely-recognized effective strategy for slowing the rate of climate warming. There are over 600,000 well-pads in the U.S.; one-fifth produce most of the economic value, while the remainder produce limited oil/gas. We use high-resolution MethaneSAT satellite data covering >80% of US onshore production to determine methane emissions across individual well-pad production cohorts, bridging a knowledge gap between what point-source and global-mapping satellites provide. The analysis reveals outsized methane emissions from low-producing well-pads (<15 boe/day), that account for only 6% of national production but more than half of well-pad methane emissions and ~40% of total oil/gas supply-chain emissions. The mean emissions intensity from low-producing well-pads is over tenfold compared to higher-producing well-pads, revealed by the spatially explicit satellite-based methane emissions intensity mapping. These low-producing well-pads represent a major methane mitigation opportunity for the U.S. oil/gas sector.


## Teaser

Satellite data reveal low-producing U.S. oil/gas well-pads contribute outsized methane emissions, offering an important mitigation opportunity.

## INTRODUCTION

Methane is a potent short-lived greenhouse gas which is responsible for ~30% of anthropogenic-caused climate warming (*1*). Reducing anthropogenic methane emissions from the global oil and gas sector is one of the most effective strategies for near-term climate warming mitigation (*2*, *3*). A wide range of measurement approaches have been developed to quantify methane emissions, spanning site-level observations to global atmospheric inversions constrained by satellite data. Recent advances in satellite remote sensing have substantially improved the spatial and temporal resolution of methane emissions data. Global mapping satellite-based systems can provide emission quantification at regional and national scales (*4*, *5*), while point-source imagers enable detection and monitoring of large facility-scale emissions (*6*, *7*). MethaneSAT (March 2024 – June 2025) was designed to bridge the observational gap between global mapping and point source observations by providing high-resolution (110 × 400 m pixel size at nadir) and high-precision measurements over wide spatial domains (~250 × 220 km average of all observations) (*8–10*), in order to quantify emissions at individual basins and jurisdictions but also spatially resolve emissions at finer area scales. Atmospheric inverse modelling of MethaneSAT observations yield methane emission rate estimates at a fine spatial scale (i.e., $4 \times 4\ km^2$), exceeding the spatial granularity of conventional bottom-up inventories which currently are available at 0.1° × 0.1° (i.e., $10 \times 10\ km^2$) (*11–14*). These advances enable the characterization of spatial heterogeneity in methane emissions at a regional scale, allowing the connection of observed emissions to underlying oil/gas infrastructure which provides policy-relevant data to better understand emissions variability at multiple spatial scales in order to support effective mitigation opportunities.

Methane emissions intensity is defined as the ratio of methane emissions normalized by gas and/or oil production. Recent initiatives, like the Oil and Gas Climate Initiative (*15*), and member companies from the Oil and Gas Decarbonization Charter who produce ~40% of global oil and gas (*16*), have set ambitious targets, such as reducing gas production-normalized methane intensity to near zero, with a benchmark of 0.2% by 2030 (*15*). However, comparing methane intensity across oil and gas basins and over time is complicated by differences in production trends, infrastructure deployed, oil and gas composition, and measurement methods. For example, satellite-based estimates show that gas production-normalized methane intensity has declined in the Permian Basin in recent years despite relatively stable total oil and gas methane emissions, even with increased total oil and gas production (*17–19*). Marginal well-pads, typically defined as producing less than 15 barrels of oil equivalent per day combined from wells within the well-pad, contribute relatively little to total energy production (*20*). Yet, marginal well-pads are numerous (over half a million in the United States) and widely dispersed across production regions in the United States (U.S.), and their emissions are often co-located with other infrastructure, including compressor stations, processing facilities, and refineries, that may emit methane at rates that do not scale with proximate production (*20–24*). As a result, regional emission estimates derived using existing global mapping satellite data at coarse-scale inversions (typically at $50 \times 50\ km^2$ or $25 \times 25\ km^2$ resolution) represent aggregate emissions from a diversity of infrastructure types and production cohorts rather than isolating specific source types. Disentangling emission contributions from the components of oil and gas production requires observations with sufficient spatial resolution to resolve area emissions from different oil/gas production cohorts including across marginally producing landscapes.

Here, we use high-resolution ($4 \times 4\ km^2$) methane emission estimates based on the high precision spectrometer measurements obtained by MethaneSAT from May 2024 to June 2025 that represent over 80% of total oil and gas production in the contiguous U.S. (CONUS) in 2024 (see Methods). We isolate areas populated by production well-pads without other associated above-ground oil and gas infrastructure (see Methods), enabling a satellite-based assessment of emissions from production-only areas. We then use the satellite-derived well-pad emissions to upscale to the entire CONUS. The goal is to quantify the relative contributions of marginal and non-marginal production to national-scale well-pad methane emissions and to examine methane emissions intensity across individual basins in terms of losses of methane relative to both gas production and total energy (oil and gas) production.

## RESULTS

### High resolution methane emissions and intensity estimates

We aggregate methane emission estimates from 74 MethaneSAT scenes and disaggregate total emissions by methane sector (SI – Fig. S1-S2; Table S1; see Methods). Within MethaneSAT-observed regions in the CONUS, we estimate total oil and gas methane emissions of 6.6 Tg $a^{-1}$ (95% CI: 5.0–8.3; Fig. 1a). These regions accounted for 84% of total onshore marketed oil and gas production in the CONUS in 2024. The aggregated emissions dataset includes 11 oil and gas basins, with >90% basin-level production coverage in nine of them (Table S5). We compare our oil and gas emissions estimates for the observed regions with recent TROPOMI inversions for 2023 (*3*) and find statistical agreement with their estimate of 6.8 Tg $a^{-1}$ (95% CI: 4.8–7.2; Fig. 1b). Our estimates are nearly twice the oil and gas emissions reported to the UNFCCC by the U.S. EPA (*11*, *12*) for similar areas (Fig. 1b), although these bottom-up estimates are for the year 2020.

We calculate methane emissions intensity normalized by gas production (“loss rates”) and combined oil and gas production (“energy intensity”) across multiple spatial scales, including basin, county, and grid-cell (~4 × 4 km) levels (see Methods). Across the full MethaneSAT observation domain in the U.S., we estimate a gas-normalized methane emissions intensity of 1.2% (95% CI: 0.8 – 1.4%) and an energy-normalized intensity of 0.12 kg $CH_4$ $GJ^{-1}$ (95% CI: 0.08 – 0.16) (Fig. 1c). These values are lower than airborne estimates from MethaneAIR (i.e., 1.6%) for 2023 covering similar but distinct oil and gas basins (*25*).

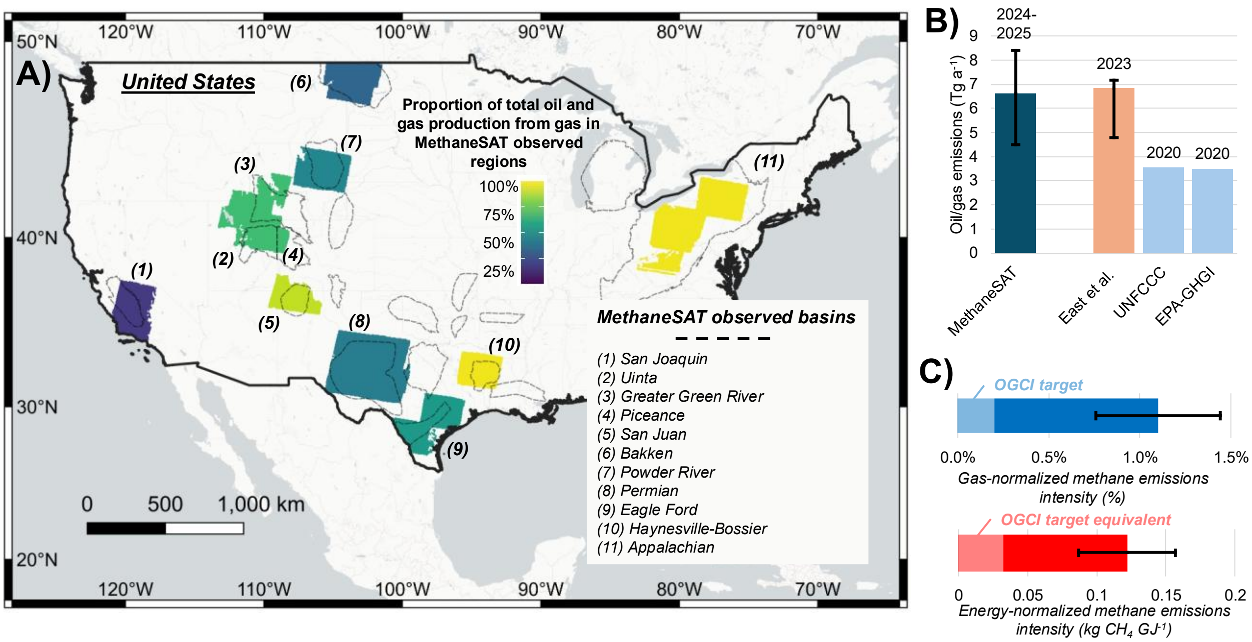


**Fig. 1. Surveyed regions by MethaneSAT and comparisons of oil/gas emissions and intensity.** a) Map of all surveyed regions by MethaneSAT in the contiguous United States (CONUS) colored by the percentage of total marketed gas production relative to total marketed oil and gas produced for the measured region in 2024 (*26*). Oil and gas basin boundaries are shown by black dashed lines for the top 20 producing oil and gas basins in the U.S., and those targeted by MethaneSAT observations are named in the legend. b) Comparisons of total supply-chain oil and gas methane emissions for surveyed regions in the CONUS (excluding end-use oil and gas methane emissions) to bottom-up (*12*, *13*) and top-down TROPOMI inversion estimates (*4*) over the same observation domains. Oil and gas estimates from the UNFCCC are obtained from spatially-resolved emissions presented in the Globel Fuel Exploitation Inventory v3 (*12*). The corresponding years of measurement are indicated above the bars. c) Methane emissions intensities for the full aggregated MethaneSAT observation domain in the CONUS. The OGCI (*15*) methane emissions intensity target of <0.2% for gas-normalized methane emissions intensity, and the equivalent energy-intensity target of <0.03 kg $CH_4$ $GJ^{-1}$ are shown for reference. The energy-intensity equivalent value of <0.03 kg $CH_4$ $GJ^{-1}$ is the gas-only equivalent energy intensity (see Methods).

Figure 2 shows maps of oil and gas production alongside methane emissions intensity estimates for the Permian, Eagle Ford, and Haynesville oil and gas basins, with the remaining observed regions shown in the SI – Fig. S3-S5. Methane emissions intensity increases systematically in lower-production areas, with the highest values occurring at the periphery of major production zones (Fig. 2b,d). This pattern reflects an inverse relationship between production and methane emissions intensity, as identified in previous work (*20*) (SI – Fig. S6). Sampling strategies can strongly influence reported methane intensities. Aerial measurement campaigns often prioritize high-production areas to capture large emission sources (*25*, *27*, *28*), which may bias intensity estimates low if low-producing areas are underrepresented. Conversely, studies focused on marginal or low-production areas may yield higher intensity estimates. Meaningful comparisons therefore require measurements over broad spatial domains encompassing the full range of emission characteristics.

Our estimates reflect the MethaneSAT observation footprint, which captures both core production areas and surrounding infrastructure across all regions analyzed.

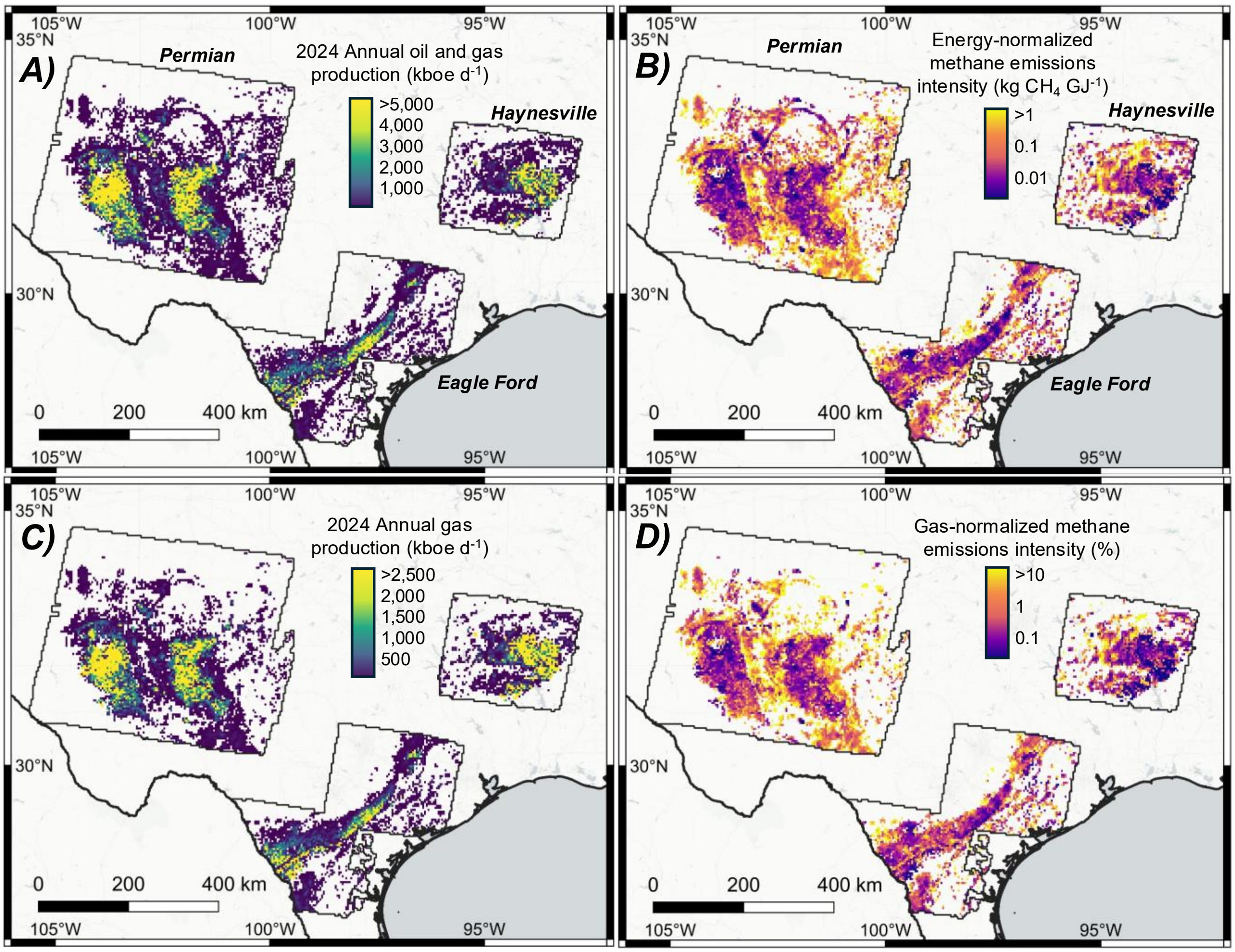


**Fig. 2. Gridded oil and gas production and methane emissions intensity.** Aggregated MethaneSAT observation domains for the Permian, Eagle Ford, and Haynesville oil and gas basins. Annual marketed 2024 **a)** gas-production and **c)** oil and gas production gridded by MethaneSAT observation grid cells (*26*). Gridded **b)** gas-normalized and **d)** energy-normalized methane emission intensities at the native $4 \times 4$ km$^2$ grid cell resolution of MethaneSAT emissions. Note that methane emissions intensity metrics in panels **b,d)** are presented in $\log_{10}$ scale. Production and intensity breakdowns are shown for other observed regions in the SI (Fig. S3-S5).

At the grid-cell level (ie., $4 \times 4$ km$^2$), only 16% of intensity estimates fall below the OGCI methane intensity target of 0.2% for loss rates, and just 11% fall below the corresponding energy-intensity equivalent target of 0.03 kg $CH_4$ $GJ^{-1}$ (Fig. 3a,c). We note substantial variability in grid-cell-level methane intensity estimates (Fig. 3a,c), regardless of whether intensity metrics are based on gas alone or combined oil and gas production. Fine resolution emissions data captures localized low-production areas and isolated infrastructure, leading to significant variability in measured emissions intensity when measured over a broad regional context. In contrast, aggregation to basin scales incorporate additional non-producing infrastructure (e.g., compressor stations and processing facilities) while encompassing increased oil and gas production with a larger coverage area, increasing both the numerator and denominator in the methane emissions intensity calculations (see Methods). Within oil and gas basins, gas-normalized methane intensities (i.e., loss rates) range from 0.5 - 0.6% in gas-dominated basins like the Appalachian and Haynesville, up to 8.9% in an oil-dominated basin like the San Joaquin (Fig. 3b,d). Elevated loss rates in regions with significant oil production can be biased high (*29*, *30*), underscoring the importance of complementary energy-normalized metrics. In contrast, the Appalachian basin which is a high gas-producing basin, consistently shows some of the lowest methane intensities in the U.S. (*25*, *27*, *31*, *32*). Using oil-and-gas-normalized methane emissions intensity (i.e., energy intensity), the lowest intensities are observed in the Bakken (0.05 kg $CH_4$ $GJ^{-1}$) and Appalachian (0.09 kg $CH_4$ $GJ^{-1}$) basins, while the highest occur in the Piceance (0.23 kg $CH_4$ $GJ^{-1}$) and San Joaquin (0.27 kg $CH_4$ $GJ^{-1}$) basins. Both our localized grid-cell analysis and basin-level assessments of methane emissions intensity highlight substantially higher emissions than the industry loss rate target of 0.2% (*15*) and energy intensity equivalent target of 0.03 kg $CH_4$ $GJ^{-1}$ (see Methods).

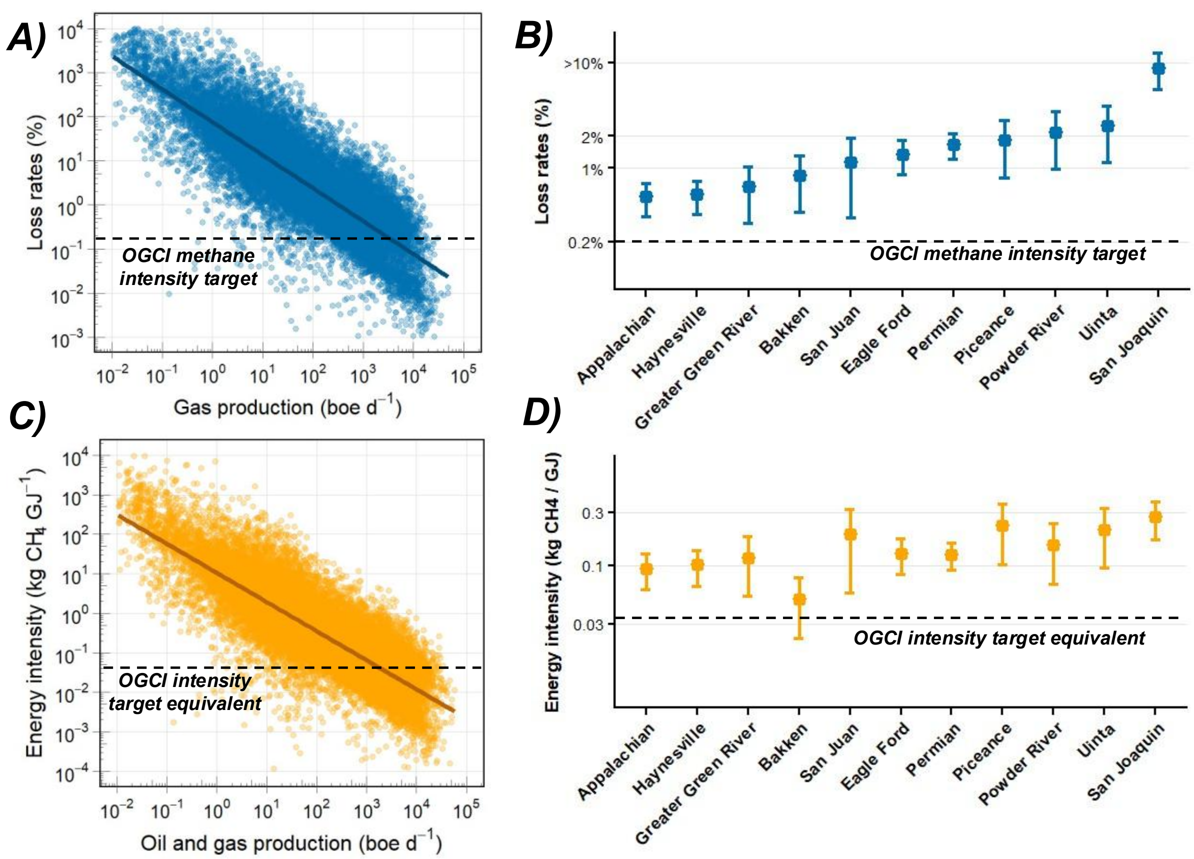


**Fig. 3. Relationships between oil and gas production and methane intensity. a,c)** Scatterplots of the entire compiled MethaneSAT dataset for the contiguous U.S. (CONUS) showing methane intensities normalized by gas- (i.e., loss rates) and combined oil and gas (i.e., energy intensity) production by all grid cells (ie., 4 × 4 $km^2$) containing actively production well-pads. **b,d)** Basin-level breakdowns of estimated methane intensities within satellite-observed oil and gas basin boundaries domains. The OGCI methane intensity target (or equivalent for energy intensity) are shown as black dashed lines throughout the panels (*15*). The OGCI energy intensity equivalent is

calculated by converting a 0.2% loss rate to a gas-only energy intensity (kg $CH_4$ $GJ^{-1}$) (see Methods).

## Production-level breakdown of observed emissions

We consolidate production from ~810,000 actively producing wellheads to ~660,000 well-pads (~1.2 wellheads per well-pad) using a spatial buffer approach that follows previously established methods (*23*, *33*), with ~545,000 marginal well-pads (~1.1 wellheads per well-pad) and ~115,000 non-marginal well-pads (~1.8 wellheads per well-pad) (see Methods). We isolate MethaneSAT observation grid cells that contain only actively producing well-pads and exclude above-ground infrastructure including VIIRS flare detections, compressor stations, refineries, processing plants, standalone tank batteries, injection and disposal sites, and LNG facilities using infrastructure data contained within the OGIM v2.7 (*34*) and Enverus (*35*), and account for emissions from transmission pipelines by subtracting estimated pipeline emissions using calculated cell-level pipeline lengths and default emission factors (see Methods). The resulting emissions data, which we refer as “wells-only grid cells” or “production-only grid cells”, effectively contain emissions directly associated with production well-pads, analogous to site-level analyses in prior work (*20*, *22*). Accordingly, results in this section should be interpreted as production-associated emissions rather than total oil and gas sector emissions, which include a broader range of oil and gas value chain related sources (e.g., compressor stations, processing facilities) (*27*).

Across the full dataset, we partition 18,650 wells-only grid cells (i.e., ~300,000 $km^2$) from 42,423 containing either a mixture of well-pads with other oil/gas infrastructure or containing no actively producing well-pads (Fig. 4) (see Methods). Methane emissions from wells-only grid cells total 3.8 (95% CI: 2.6 – 4.9) Tg $a^{-1}$ before subtracting 0.1 Tg $a^{-1}$ estimated for transmission pipelines (see Methods). The wells-only grid cells represent 31% of the total area surveyed but 58% (95% CI: 45 - 76) of the total oil and gas emissions from the entire satellite observation domain (Fig. 4).

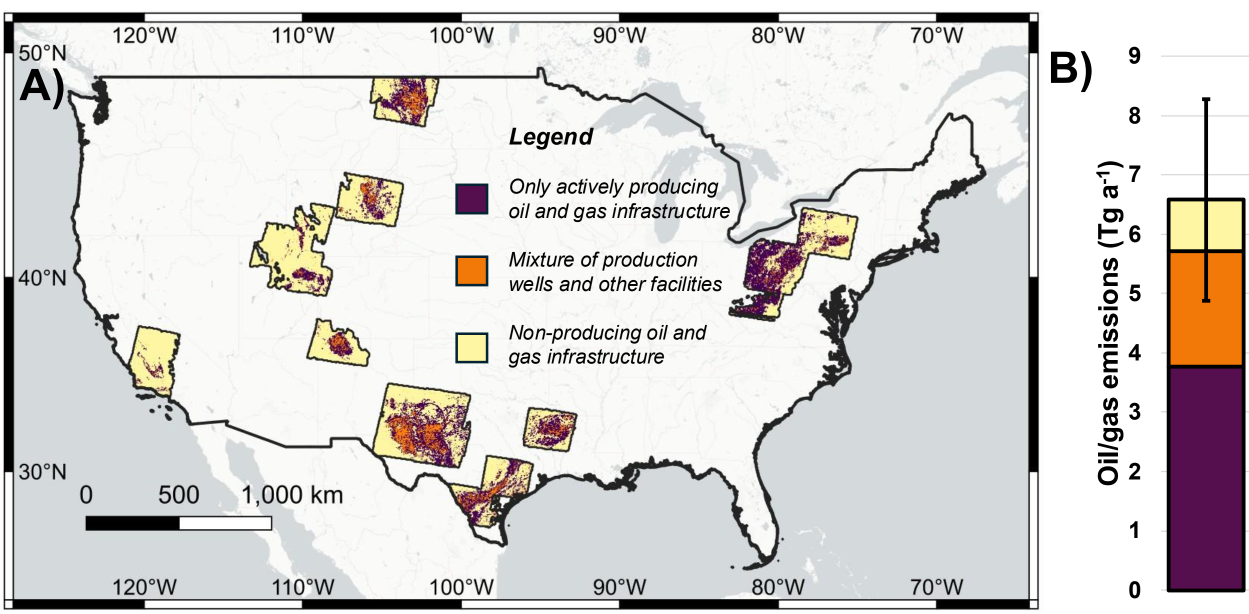


**Fig. 4. Distribution of MethaneSAT emissions categorized by underlying infrastructure.** a) Distribution of methane emissions from oil and gas infrastructure within MethaneSAT observation grid cells for all observed regions in the CONUS. Production-only grid cells (purple) contain actively producing oil and gas well-pads but exclude VIIRS flare detections, compressor stations, refineries, processing plants, standalone tank batteries, injection and disposal sites, and

LNG facilities. Grid cells containing a mixture of actively producing well-pads and the other oil and gas infrastructure are shown in orange, and those containing oil and gas methane emissions but no actively producing well-pads are shown in yellow. b) Total oil and gas emissions from production-only grid cells, cells containing a mixture of production well-pads and other infrastructure, and grid cells containing no actively producing well-pads but other related oil and gas infrastructure.

The infrastructure-based spatial filtering approach we utilize in this work is possible because of the fine spatial resolution of the underlying satellite observations (ie., native pixel size of $110 \times 400$ $m^2$) and the high precision of the data which enable the high-resolution satellite inversion emissions estimates. As the resolution of gridded emissions data coarsens the cells aggregate multiple infrastructure types which results in the consideration of ever smaller proportions of production (Fig. S7). This analysis (i.e., wells-only grid cells) includes 45% of all actively producing well-pads in the CONUS, and 44% of total CONUS oil and gas production. Using the MethaneSAT observation regions in the CONUS as a baseline, the percentage of total well-pads retained within wells-only grid cells decline by 76% when the resolution is coarsened to $25 \times 25$ $km^2$ and declines even further at resolutions of $50 \times 50$ $km^2$ (ie., -94%) and $100 \times 100$ $km^2$ (ie., -99%) (Fig. S7). To our knowledge, the finest resolution of global/national satellite emission inversions currently available in literature is $25 \times 25$ $km^2$ (*4*), but note that some basin-level assessments using TROPOMI data have been reported at $10 \times 10$ $km^2$ resolution (*18*).

We normalize total production by the counts of active well-pads, yielding an average production-per-well-pad metric at the $4 \times 4$ $km^2$ grid-level scale. Grid cells are classified as marginal or non-marginal based on whether average well-pad production is below or above 15 boe $d^{-1}$ well-pad$^{-1}$. This approach provides a zonal representation of production intensity rather than individual well-pad production. Across all observations, wells-only grid cells contain an average of 15.2 well-pads grid cell$^{-1}$ (median 6; range 1 – 1,780), indicating spatial heterogeneity in well-pad density. Within the satellite observation boundaries, marginally producing grid cells are most prevalent with 12,319 versus 6,331 non-marginal grid cells (Table 1). Marginal grid cells contain a total of 217,000 actively producing well-pads, with 95% of them being marginally producing. Non-marginal grid cells contain a total of 65,700 well-pads with 52% being non-marginal well-pads. Despite containing a higher count of well-pads, marginally-producing grid cells account for only 5% of total production within this partitioned dataset. Overall, our wells-only dataset represents methane emissions data from over 280,000 well-pads.

**Table 1. Description of wellhead and well-pad infrastructure data within MethaneSAT observed regions.** Infrastructure breakdown of active production well-pads and wellheads contained within marginally- and non-marginally producing grid cells. All statistics are presented for the measured wells-only areas within MethaneSAT observation boundaries. Total counts of

well-pads, and wellheads, may not equal the sum of the marginal and non-marginal classifications due to rounding.

| | **Marginal grid cells (n = 12,319)** | **Non-marginal grid cells (n = 6,331)** |
|---|---|---|
| # total well-pads | 217,000 | 65,700 |
| # marginal well-pads | 207,000 | 31,600 |
| % marginal well-pads | 95% | 48% |
| # non-marginal well-pads | 10,000 | 34,100 |
| % non-marginal well-pads | 5% | 52% |
| Avg. count of marginal well-pads per grid cell | 16.8 | 5.0 |
| Avg. count of non-marginal well-pads per grid cell | 0.8 | 5.4 |
| # total wellheads | 240,000 | 102,000 |
| # total marginal wellheads | 227,000 | 35,500 |
| # total non-marginal wellheads | 12,100 | 66,100 |
| % of total production within combined wells-only grid cells | 5% | 95% |

We first calculate the relative contributions of marginally-producing grid cells to all wells-only grid cells in each MethaneSAT observed region after the subtraction of estimates methane emissions from transmission pipelines (see Methods). We find that marginally producing grid cells contribute 1.8 Tg $a^{-1}$ (95% CI: 1.3 – 2.3) of methane, accounting for approximately 49% (95% CI: 34 - 64%) of all production-only grid cells, with the remaining 51% (95% CI: 36 - 66%) from higher-producing grid cells (Fig. 5a). A stratified bootstrap analysis (n = 1,000) confirms that the partitioning between marginal and non-marginal grid cells is robust, yielding a median marginal contribution of 49% (95% CI: 47 – 51%) (Fig. S8). A permutation test further confirms that the observed emission split significantly deviates from expectations under random allocation given group sizes ($p < 0.001$), indicating that emissions are disproportionately distributed across production classes (Fig. S9). Using our observed wells-only grid cells, we estimate national methane emissions from the production sector for the entire CONUS and the associated proportion of emissions from marginally-producing areas (see Methods), with further extrapolation to marginal well-pad contributions informed by simulation results presented in the SI – Section 1.

**Well-pad emissions in the contiguous U.S.**
We estimate total methane emissions from well-pads in the CONUS to be 9.6 Tg $a^{-1}$ (95% CI: 6.8 – 12.4) from the observed wells-only grid cells and the national extrapolation informed by the MethaneSAT estimates. Our estimate of total well-pad emissions statistically agree with 2021 bottom-up estimates of 9.6 Tg $a^{-1}$ (*23*) and 9.9 Tg $a^{-1}$ (*24*) that were based on facility-level extrapolations from ground-based measurements. Our estimated well-pad emissions account for 72% (95% CI: 42 - 93) of total oil and gas supply chain emissions in the CONUS (excluding end-use) based on TROPOMI estimates for 2023 (*4*) (Fig. S16), highlighting the production sector as the largest contributor to total methane emissions from the oil and gas supply chain (*13*, *23*, *24*, *27*, *36*). Based on our estimated well-pad emissions in the CONUS, the equivalent gas-normalized methane intensity (ie., loss rate) is 1.2% (95% CI: 0.9 – 1.6) with an energy intensity value of 0.14

kg $CH_4$ $GJ^{-1}$ (95% CI: 0.10 – 0.19). Our estimated loss rate for the production sector is statistically similar to production sector loss rates of 1.3% (*27*) for 2015, which reflects the associated growth in oil and gas production coupled with increased methane emissions (*37*). We estimate the contribution from marginally-producing areas in the CONUS to be 5.1 Tg $a^{-1}$ (95% CI: 3.3 – 6.8), or 53% (95% CI: 34 - 72) of the total CONUS well-pad emissions (Fig. 5b). Marginally-producing areas have high methane intensities with an estimated loss rate of 13.0% (95% CI: 8.5 – 17.6) and energy intensity of 1.44 kg $CH_4$ $GJ^{-1}$ (95% CI: 0.94 – 1.94), much higher than those from non-marginally producing areas which have a loss rate of 0.6% (95% CI: 0.4 – 0.9) and an energy intensity of 0.07 kg $CH_4$ $GJ^{-1}$ (95% CI: 0.05 – 0.10). Aggregating point-level (i.e., well-pad) production into area-normalized values can introduce discrepancies when partitioning cumulative emissions by area-based thresholds (e.g., ≤15 boe $d^{-1}$ well-$pad^{-1}$) (*38*, *39*), therefore we estimate emissions for well-pads and their respective production cohorts (see SI – Section 1).

To assess the actual contribution of marginal well-pad emissions, as opposed to the marginally producing areas based on our satellite observations, we perform a series of simulations to estimate the difference between the gridded and well-pad proportions (see SI - Section 1). We find that our grid-cell based estimates underestimate the contribution from marginally producing well-pads by 5% (95% CI: 2 – 7) based on our simulation results (Fig. S19; SI – Section 1), which corresponds to a contribution of production-related emissions from marginal well-pads of 58% (95% CI: 36 – 79), or 5.6 Tg $a^{-1}$ (95% CI: 3.5 – 7.6). The methane emissions intensities for marginal well-pads in the CONUS equate to a loss rate of 16% (95% CI: 10 – 23) and an energy intensity of 1.84 kg $CH_4$ $GJ^{-1}$ (95% CI: 1.10 – 2.57). In parallel, we estimate total methane emissions from non-marginal well-pads at 4.0 Tg $a^{-1}$ (95% CI: 2.1 – 6.4), which translates to a loss rate of 0.6% (95% CI: 0.3 – 0.8) and an energy intensity of 0.07 kg $CH_4$ $GJ^{-1}$ (95% CI: 0.04 – 0.09). Based on total supply-chain methane emission estimates from TROPOMI satellite inversions for 2023 (*4*), the contribution of marginal well-pads would be approximately 39-42% for the CONUS from our estimated area-based or marginal well-pad emissions, respectively (Fig. S16). Our area-normalized approach underestimates total marginal-well-pad emissions across the CONUS because the ~91,000 marginal well-pads sitting in non-marginal areas outnumber and outweigh (in emissions) the ~22,000 non-marginal well-pads sitting in marginal areas, a redistribution driven mainly by site counts rather than production levels (Table S6; SI – Section 1). Marginal well-pads emit methane at lower absolute rates on average than higher producing well-pads (*20*, *22–24*), but collectively their large numbers lead to significant methane emissions, despite their limited contributions to total energy production.

We find that marginally producing well-pads account for over half of all production-related methane emissions yet produce only 6% of total national oil and gas production (Fig. 6; Fig. S18). At other production thresholds, ultralow producing well-pads (<2 boe $d^{-1}$) contribute 28% (95% CI: 17 - 40) of total production-related emissions and 0.6% of total production, whereas high-producing well-pads (>300 boe $d^{-1}$) contribute 14% (95% CI: 9 - 19) of total well-pad emissions and 77% of total CONUS production (Fig. 6; Fig. S18). These proportions of production-related emissions are statistically similar to our grid-cell level estimates from ultralow producing areas (<2 boe $d^{-1}$ well-$pad^{-1}$) at 21% (14 - 28) and from high-producing areas (>300 boe $d^{-1}$ well-$pad^{-1}$) at 13% (8 - 18). We estimate the corresponding methane intensities from ultralow producing well-pads in the CONUS at 60% (95% CI: 36 – 86) for loss rates and 6.66 kg $CH_4$ $GJ^{-1}$ (95% CI: 4.04 – 9.52) for energy intensity, more than double the methane intensities from marginal well-pads. The methane intensities from high-producing well-pads (i.e. >300 boe $d^{-1}$ well-pad$^{-1}$) are 0.2% (95% CI: 0.1 – 0.3) for loss rates and 0.03 kg $CH_4$ $GJ^{-1}$ (95% CI: 0.02 – 0.04) for energy intensities.

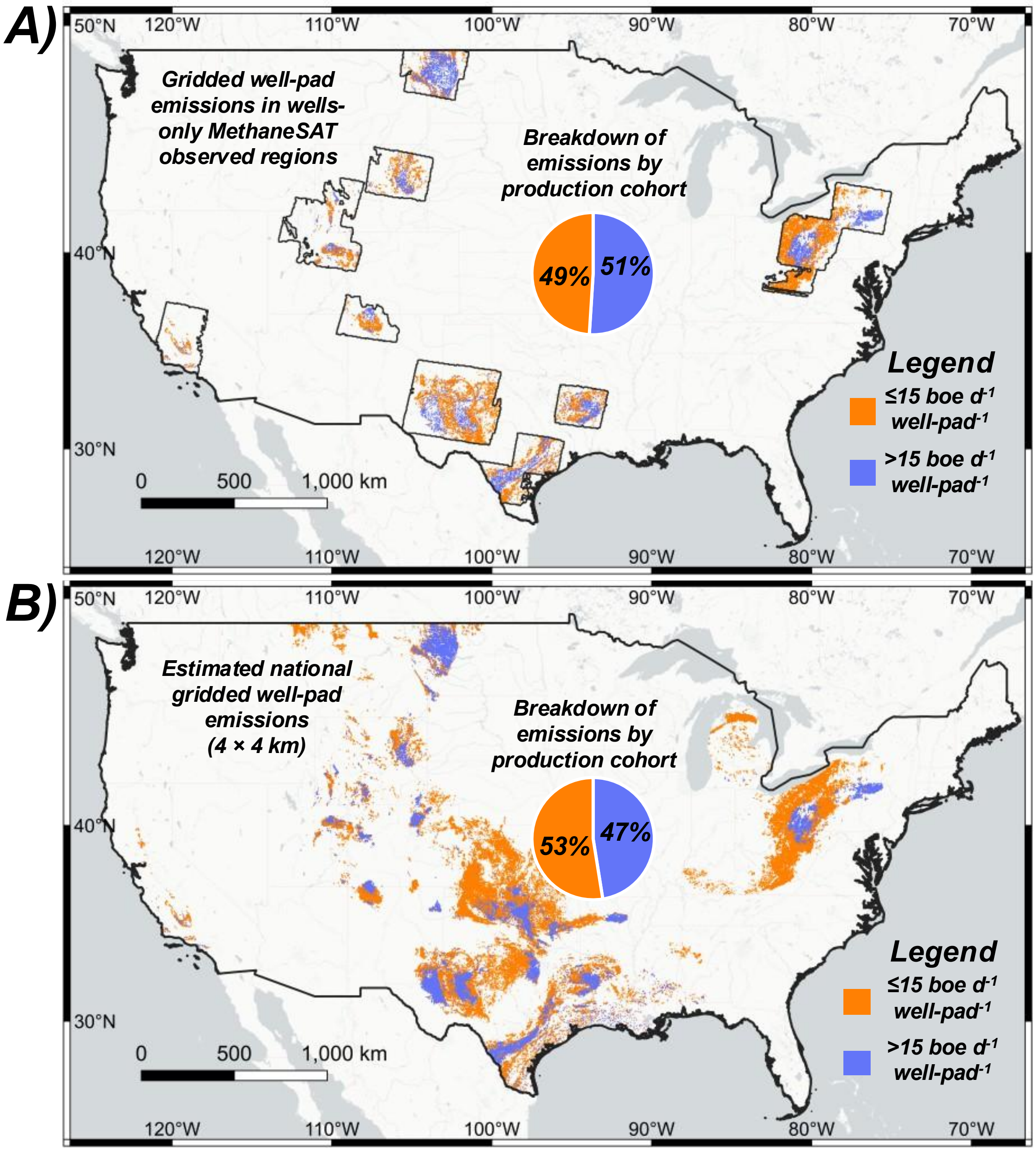


**Fig. 5. Methane emissions from marginal and non-marginal areas in the CONUS. a)** Map of aggregated MethaneSAT wells-only observations in the contiguous U.S. (CONUS) highlighting marginally- (orange) and non-marginally-producing (blue) grid cells. Wells-only grid cells are limited to actively producing oil and gas infrastructure, and production is normalized by the number of actively producing well-pads to determine whether a grid cell is marginally- (≤15 boe $d^{-1}$ well-pad$^{-1}$) or non-marginally producing. **b)** Gridded well-pad emission estimates extrapolated to the entire CONUS using MethaneSAT data (see Methods). Pie charts in both panels show the relative contributions of area-normalized marginally- (orange) and non-marginally producing-well-pad emissions (blue). This estimate does not include the ~7% underestimate for the national proportion

of emissions from marginal well-pads emissions which is introduced by using the area-normalization of well-pad production (SI – Section 1).

## Comparisons to independent measurements and sensitivity testing

Across oil and gas basins, we find that the proportion of emissions from marginally producing grid cells varies substantially (Fig. S10). In the Permian basin, we estimate total well-pad emissions of 2.0 Tg $a^{-1}$ (95% CI: 1.4 – 2.6) with 33% (95% CI: 23 – 44) of well-pad emissions from marginally-producing grid cells (Fig. S10), which statistically matches independent estimates from an aerial LiDAR sampling campaign for 2024 (*40*) (Table S3) who find 35% of emissions from marginally producing well-pads. In contrast, for the Appalachian basin we estimate total well-pad emissions of 1.5 Tg $a^{-1}$ (95% CI: 0.9 – 2.2) with 70% (95% CI: 47 – 93) of well-pad emissions from marginally-producing grid cells. Our estimates in the Appalachian basin statistically overlap with independent multi-scale facility-level estimates that find 78% of total well-pad emissions from conventional well-pads, which are predominantly marginally-producing (*41*). Overall, the inter-region differences highlight the need for regionally tailored mitigation strategies.

Using our adjusted estimate of emissions from marginally producing well-pads in the CONUS from our simulation results (see SI – Section 1), we estimate an average emission rate for marginally producing well-pads of 1.2 kg $h^{-1}$ (95% CI: 0.7 - 1.6), which is statistically consistent with previous estimates of marginal well-pad emissions in the U.S. using facility-level ground-based estimates (i.e., 0.8 - 0.9 kg $h^{-1}$ per marginal well-pad) (*20*) and airborne measurements in the Permian Basin (0.9 kg $h^{-1}$ per marginal well-pad) (28). The average emission rate from non-marginally producing well-pads is higher at 4.0 kg $h^{-1}$ per well-pad (95% CI: 2.1 – 6.5), which statistically agrees with emission factors for non-marginal well-pads at 4.9 kg $h^{-1}$ well-pad$^{-1}$ (95% CI: 3.5 - 7.1) from the EI-ME (*23*). Based on well-pad normalized emission rates, approximately 88% of our observed well-pad emissions originate from grid cells with emissions <100 kg $h^{-1}$ well-pad$^{-1}$, but we note that these estimates assume that emissions are distributed equally among well-pads within a given grid cell. Based on our results, and other studies as well (*20*, *22–24*), capturing close to a majority of cumulative emissions from marginal well-pads through point-source imaging satellite systems alone would be challenging given their current detection thresholds which typically fall in the range of 100 - 1,000 kg $h^{-1}$ with >50% detection probability (4, 33–35).

We find that the proportion of well-pad emissions from marginally producing areas, which provide the basis for our well-pad estimates, remains stable throughout extensive sensitivity testing, which is presented in detail in the SI – Section S2. For the first test, we restrict the MethaneSAT observed data only to areas contained in three or more overpasses and use the associated data to estimate the proportion of well-pad emissions from marginally producing areas. Next, we classified grid cells from individual MethaneSAT inversions as marginally and non-marginally producing and calculated correlations between the Markov chain Monte Carlo posterior samples (n = 4,000) of each emitter within the group and those of every emitter outside it (see Methods). Emitters exhibiting a correlation below −0.1 with any out-of-group emitter were considered insufficiently separable for definitive source attribution and were excluded in the sensitivity analysis. We also mapped the posterior-predicted enhancements attributable to each group (ie., marginal- or non-marginal areas) and their contributions to the total enhancement, enabling identification of large emission sources with poorly distinguishable atmospheric signatures (SI – Figure S9).

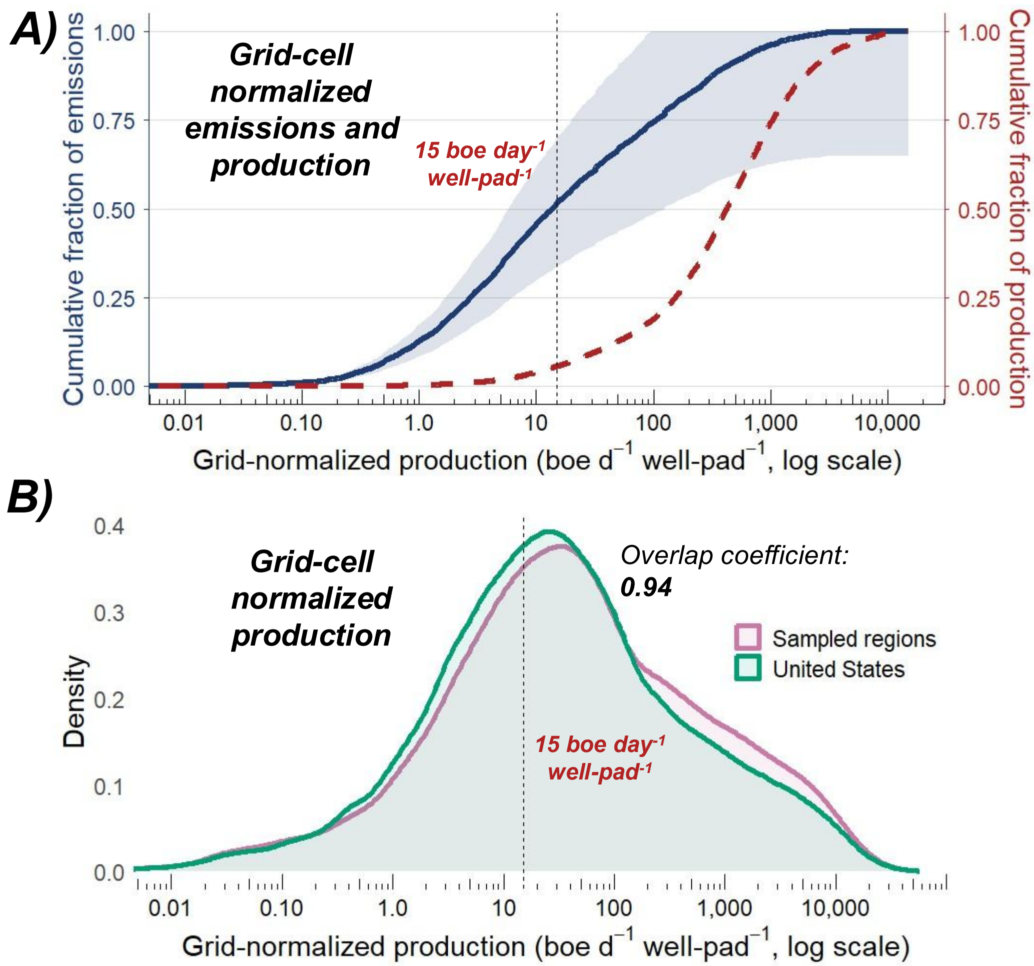


**Fig. 6. Cumulative methane emissions by cumulative production in the CONUS. a)** Plot of cumulative methane emissions and oil and gas production by well-pad normalized production from our measured well-pad emissions to the entire contiguous United States (CONUS). Shaded regions for the cumulative emissions represent the 95% confidence intervals on the estimated emissions proportion. **b)** Density plots showing the population of grid-cell normalized production for all the onshore CONUS and the sampled regions by MethaneSAT. The overlap coefficient indicates the degree of agreement between both density distributions, with a value of 1 indicating perfect agreement.

## DISCUSSION

We present a satellite-based methane emissions analysis across the CONUS, covering more than 80% of national oil and gas production in 2024. High-resolution mapping of methane emissions intensity, normalized by gas production and by combined oil-and-gas production, reveals disproportionately large methane intensities in marginal production areas outside major basin production zones. Despite only producing 6% of oil and gas methane emissions, marginal production well-pads account for 58% of emissions from all well-pads, at the aggregated grid level the attribution is 53% from marginally producing areas. Marginal well-pads are far more numerous, emit less methane per site, and contribute minimally to total energy production compared with well-pads producing above 15 boe $d^{-1}$ well-pad$^{-1}$, yet both types contribute roughly equally to total production-related methane emissions. Collectively, these results show that marginal production well-pads make a substantial and consistent contribution to oil and gas methane emissions across scales and region.

This satellite-based, spatially explicit constraint corroborates earlier site-level findings that marginal well-pads contribute disproportionately to production-related emissions relative to their production (*20*, *22*). Informed by simulation results (see SI - Section 1), marginal well-pads show a methane loss rate of 16% and an energy intensity of 1.8 kg $CH_4$ $GJ^{-1}$, more than an order of magnitude higher than non-marginal well-pads, for which we estimate a loss rate of 0.6% and an energy intensity of 0.07 kg CH4 $GJ^{-1}$, less than half the sector-wide average. This elevated intensity marks marginal well-pads as a critically important, underappreciated mitigation target. Given their large numbers and diffuse spatial distribution (>500,000 marginal well-pads across the CONUS), effective abatement will likely require broad, systemic approaches. Ultralow-producing well-pads (<2 boe $d^{-1}$) magnify the challenge, contributing roughly a fifth of total well-pad emissions while producing less than 1% of national oil and gas. Inversely, high-production well-pads (>300 boe $d^{-1}$) produce almost 80% of total CONUS production but have associated methane emission intensities that are nearly an order of magnitude lower than the national average.

Our analysis is grounded in the ability of fine-resolution satellite emission inversion data to isolate areas solely containing production well-pads. As the resolution of the spatially-explicit methane emissions data coarsens, the quantity of data retained using this spatial filtering approach reduces (i.e., areas solely containing production well-pads). This is evident even at the resolution of 25 × 25 km$^2$ currently the basis for global satellite mapping based inversion studies (*4*), where we note a large drop of ~75% in the available wells-only emissions data compared to the MethaneSAT inversion resolution of 4 × 4 km$^2$ (Fig. S7) suggesting the effectiveness of resolving emissions granularity and marginal production contributions at the ~4 km area scales. Comparing our analyses to comprehensive site-level sampling campaigns in the Permian and Appalachian basins (*40*, *41*), suggests that our high-resolution satellite inversion approach accurately captures the emissions contributions among production cohorts (Table S3). Simulation results presented in the SI - Section S1 further show that coarser-resolution emissions data would increase uncertainty and lower the quality of resulting well-pad analyses, underscoring the value of high-resolution observations for the granular type of analysis presented in this study in terms of quantifying the relative emission contributions from marginal and non-marginal production regions.

## MATERIALS AND METHODS

### Description of MethaneSAT's L4 area emissions data

MethaneSAT's atmospheric inversion pipeline produces gridded methane emission estimates at 0.04° × 0.04° (~4 × 4 km²) resolution, covering domains on the order of 220 × 200 km² per satellite pass. Measurements come from a pair of Littrow-design imaging spectrometers onboard the satellite, which retrieve the column-averaged dry-air mole fraction of methane ($XCH_4$) at a native nadir footprint of roughly 110 × 400 m, achieving 2.5–5.5 ppb precision when aggregated to 2 × 2 km² (*9*, *10*). To convert these column measurements into emission rates, we apply the Column Observations to Regional Emissions (CORE) framework (*45*), which underlies the

MethaneSAT Level-4 (L4) emissions product. A full detailed description of the CORE inversion framework is available from the Algorithm Theoretical Basis Document (*45*), and summaries of the method are also described in previous work (*46*). CORE links the observed methane field to underlying surface fluxes through a linear observation model:

$$z = \mathbf{J}_{int} s_{int} + \mathbf{J}_{ext} s_{ext} + (z_{prior} + Ab) \tag{1}$$

Here, $z$ denotes the observed $XCH_4$ values, J is the Jacobian encoding each observation's sensitivity to surface emissions, $s$ gives the emission rates in the interior and exterior portions of the domain, $z_{prior}$ is the prior column value carried over from the Level-2 retrieval, $A$ is the retrieval's averaging kernel, and $b$ is a fitted background offset. The Jacobian **J** (i.e., the transport operator connecting emissions to concentrations) is built from the Stochastic Time-Inverted Lagrangian Transport (STILT) model (*47*, *48*), driven by Global Forecast System meteorology (*49*). STILT simulates backward particle trajectories from observation locations to quantify the sensitivity of each observation to upwind methane emissions. STILT works backward in time, releasing particles from each observation location to trace which upwind areas influence that measurement. Footprints are computed up to 28 hours into the past, matching the approximate atmospheric ventilation timescale for domains of this size under typical wind speeds; emissions are treated as constant over this window. Prior emission rates are obtained from global mean methane emissions from all sectors at $25 \times 25$ km$^2$ resolution from East et al. (*4*), while retaining a minimum emission rate of 1 kg h$^{-1}$ km$^{-2}$ which allows the CORE inversion methodology to identify emissions anywhere, without overreliance on the prior.

Prior to inversion, Level-3 $XCH_4$ observations are averaged onto a $2 \times 2$ km² grid to suppress noise and limit computational demand. The inversion then solves for emissions at $4 \times 4$ km² resolution across an interior region defined by contiguous valid observations, while also accounting for possible emission sources up to 300 km outside this region to capture inflow from upwind sources. Background methane concentrations are modeled as the Level-2 retrieval prior plus an additive offset term, weighted by the corresponding averaging kernel (*9*). To keep the exterior source space computationally tractable, candidate exterior sources with similar atmospheric transport signatures (i.e., similar footprints) are grouped together before inversion.

We estimate the full parameter vector $\theta = (s_{int}, s_{ext}, b)$. within a Bayesian framework, drawing posterior samples via Hamiltonian Monte Carlo — specifically, the No-U-Turn Sampler (*50*) as implemented in Stan (*51*). Measurement error is modeled as Gaussian with an 11 ppb standard deviation, and all emission rates carry lognormal priors. Grid-cell fluxes are reported as posterior means, while uncertainty on total emissions across the aggregated domain reflects the 95% credible interval computed from 4,000 posterior draws. We additionally inflate this uncertainty by 20% to account for structural uncertainty in the GFS meteorological fields used to drive the transport model.

**MethaneSAT scene aggregation and sectoral disaggregation**

We aggregate methane emissions estimates from 74 individual MethaneSAT retrievals (Table S1). MethaneSAT L4 inversions are produced on a UTM coordinate grid to ensure that emitter cells are mapped to a precise $4 \times 4$ km² cell extent. For scenes within the same region which can cover multiple UTM zones, a common UTM grid is used to ensure that overlapping cells from

multiple retrievals in the same region will match. For grid cells containing multiple overlapping scenes we take the mean of emission estimates as the given emissions for that grid cell. The final aggregated MethaneSAT emissions estimates represent a heterogeneous, scene-weighted average of all available observations within each region. We reproject aggregated MethaneSAT emissions estimates to a global 4 × 4 $km^2$ grid to facilitate our estimates of total CONUS well-pad methane emissions from gridded production data. This reprojection introduces slight spatial distortions in the reprojected emissions data relative to the original MethaneSAT emissions data (ie., <1 km spatial distortion) but has no impact in our estimated methane emissions.
Individual scenes are temporally asynchronous (spanning up to ~28 hours) and spatially discontinuous, such that the aggregate reflects an ensemble of independent emission snapshots rather than a continuous or uniformly sampled field.

We allocate methane emissions to sectors using a similar methodology to Williams et al. (*8*). Briefly, we proportionally allocate total methane emissions by sector using information from a composite prior inventory. In the US, the composite prior inventory incorporates oil and gas emissions estimates from the EI-ME (*52*) and the gridded EPA-GHGI (*13*) inventories, non-oil and gas emissions estimates from the EPA-GHGI and EDGAR. We additionally incorporate wetland emissions from WetCHARTs v1.3.1 (*53*) and persistence-weighted point source emissions with a minimum of three valid overpasses from Carbon Mapper (*43*). All inputs to the composite prior inventory are mapped at a resolution of 10 × 10 $km^2$, except for WetCHARTs v1.3.1 which is mapped at a resolution of 50 × 50 $km^2$. We find that this combination of inputs into the composite prior provides a balance between temporal proximity to the study period (2024–2025), methodological diversity, comprehensive sectoral coverage, and optimized agreement with a compilation of literature-based estimates across all regions.

**Uncertainty quantification and consideration of scene counts**

Several distinct factors contribute to uncertainty in estimated methane emissions from the CORE inversion products. Transport uncertainty enters through the meteorological inputs used to build the STILT-derived Jacobian linking surface fluxes to observed concentrations. Measurement noise is not purely random but includes spatial patterns such as striping across the observation swath. Additional uncertainty stems from how well the background methane concentration is characterized, and from the inherent difficulty of separating signal from emissions located inside the domain versus inflow crossing the boundary from outside it. Finally, the inversion itself yields a distribution rather than a single value for each grid cell, with the spread of MCMC samples reflecting posterior uncertainty in the emission rate. Together these factors shape the cell-level posterior distributions that underlie all downstream uncertainty calculations.

We propagate uncertainty through the aggregation step using Monte Carlo resampling, which avoids assuming a functional form for the combined distribution. Each 4 × 4 km² cell carries 4,000 posterior draws from its individual MCMC inversion. For cells covered by more than one overlapping retrieval, we build an aggregated posterior by randomly drawing one sample from each contributing map and averaging them, repeating this process 4,000 times to construct a full empirical distribution for the combined estimate. This is done separately for every subregion defined by a unique overlap pattern among the retrievals. From the resulting aggregated distributions, we take the 95% empirical interval as our uncertainty bound on total emissions (n = 4,000), then widen this by an additional 20% to reflect structural uncertainty in the static GFS meteorological parameters feeding the inversion.

Sectoral attribution carries its own uncertainty, which we quantify through bootstrap resampling of the underlying prior emissions data. Rather than relying on a single set of prior estimates, we generate 4,000 randomly resampled versions of the combined multi-inventory prior and repeat the sector-allocation calculation for each. Bottom-up inventory contributions are treated as normally distributed at the grid-cell level with a 50% standard deviation, applied uniformly regardless of sector, while Carbon Mapper point-source contributions are resampled using each source's own reported uncertainty under a normal-distribution assumption. Running the attribution calculation across all 4,000 realizations produces an empirical distribution of sector-level emissions, from which we take the 2.5th and 97.5th percentiles as bounds. This approach captures uncertainty both in the input prior data itself and in how that uncertainty carries through into the final sectoral breakdown.

To test the temporal sensitivity of the aggregated MethaneSAT emissions, we calculate correction factors to account for seasonal patterns in oil and gas methane emissions (Fig. S11) (*17*, *19*, *54*). We calculate adjusted emissions estimates for all regions using monthly TROPOMI estimates for 2022 (*54*) to evaluate whether the MethaneSAT estimates could be seasonally biased compared to annual average estimates (Table S4). We do not account for diurnal variations in oil and gas methane emissions, although we note that previous studies have demonstrated that oil/gas methane emissions can be 25% higher during worktime hours (0900 – 1700 CST) compared to the full 24-hour emissions average (*55*).

**Methane emissions intensity calculations**

We map methane intensities normalized by both gas-production and combined oil and gas energy production at the native 4 × 4 $km^2$ resolution of MethaneSAT retrievals. Oil and gas production is compiled to individual grid cells by summing the well-level annual production values from 2024 in the U.S. using data from Wood Mackenzie (*26*). Production data for New York and Kentucky were not available for 2024 at the time of this analysis, and therefore we use 2023 production for wells within these states and note that overall production contributions of these states is minimal (ie., <0.5% of total CONUS production). Production data from Wood Mackenzie represents marketed oil and gas production (i.e., total hydrocarbons available for sale), which differs from gross oil and gas production (i.e., total hydrocarbons extracted at the wellhead). Well-pads can encompass single wellheads (or "wells") or multi-well pads depending on the location. We use a similar methodology as Omara et al (*33*) to group wellheads to well-pads and apply the same infrastructure count normalization approach to obtain well-pad-averaged production per grid cell (i.e., boe $d^{-1}$ well-$pad^{-1}$). We aggregate production from wellheads to well-pads using a 25- or 50-meter spatial buffer depending on whether a well is vertically- or horizontally-drilled, respectively. We classify a well as horizontally-drilled if the distance from the top-hole to bottom-hole coordinates exceed 250 meters. For the San Joaquin region, we apply a 20-meter spatial buffer to wellheads, which follows the methods of previous work (*33*).

We use the term methane emissions intensity to define oil and gas methane emissions normalized by gas production (i.e., loss rate) and combined oil and gas production (i.e., energy intensity), noting that multiple definitions of methane emissions intensity exist (*29*, *30*). Both loss rates and energy intensities, as defined below, are distinct yet complimentary metrics and consistent with international benchmarks used to measure progress towards methane mitigation in the oil and gas sector (*56*, *57*). We calculate loss rates as the percentage of methane emitted relative to total gas production, which requires an assumption of the methane composition in natural gas which can vary by basin (*58*). For marketed gas production, we assume a blanket methane composition in natural gas of 90% which reflects additional gas processing steps (e.g., removal of condensates, water, and acid gases like hydrogen sulfide) before ready for market. For additional conversions, we assume a value 6 $Mcf^3$ per 1 boe of gas and a methane density of 0.0192 kg $ft^3$ assuming standard engineering conditions in the United States (ie., 15.6°C and 14.7 psi). We estimate energy intensity in units of kg $CH_4$ per GJ of energy produced using the combined oil and gas production statistics assuming a conversion of 5.71 GJ of energy per 1 boe of oil and gas. The calculation of energy intensity does not require assumptions on the methane composition in natural gas. As a baseline mitigation target, we adopt the methane loss rate of <0.2% specified by the Oil and Gas Climate Initiative (OGCI) (*15*, *16*), corresponding to an energy intensity of <0.03 kg $CH_4$ $GJ^{-1}$ for gas. The equivalent oil-based energy intensity is <0.02 kg $CH_4$ $GJ^{-1}$. We calculate both methane emissions intensity metrics for varying spatial extents (i.e., basin boundaries and grid-level) by summing well-level production and the corresponding methane emissions to the domain of interest. For calculations within oil and gas basin boundaries, we geospatially clip emissions to the overlap domain to the full oil and gas boundary. We summarize the basin-level production captured by the satellite observations in the SI – Table S5.

**Analysis of well-pad emissions**

For our analysis of production-only methane emissions, we omit any grid cells that contain aboveground oil and gas infrastructure which includes gathering and transmission compressor stations, sites associated with fluid injection and disposal, LNG facilities, VIIRS flare detections, refineries, processing plants, and stand-alone batteries. We use infrastructure data from Enverus, Wood Mackenzie, and the Oil and Gas Infrastructure Mapping Project (OGIM) v2.7 (*34*). We account for emissions from transmission pipelines by multiplying a default emission factor of 0.12 kg $h^{-1}$ $km^{-2}$ with active pipeline lengths from Enverus (*35*) to estimate transmission pipeline emissions, which we subtract from our estimated grid-level emissions. We consider gathering pipelines to be associated with production and therefore do not subtract their emissions. Emissions from abandoned wells and other oil and gas sources (e.g., non-producing infrastructure (*42*)) are not incorporated into this calculation. The resulting data contains spatially explicit methane emissions data contributed solely from oil and gas production facilities, or production-only grid cells.

We normalize oil and production within the production-only grid cells by dividing total production by the count of actively producing well-pads to estimate well-pad-averaged production per grid cell. Using the well-pad-averaged production metric, we separate grid cells with production below and above 15 boe $d^{-1}$ well-$pad^{-1}$ to obtain marginally and non-marginally producing grid cells. We use the term grid cell to identify a single 4 × 4 $km^2$ emission value from MethaneSAT, and the term "area" to identify an aggregate of multiple grid cells. We perform additional sensitivity tests to evaluate the potential differences between actual well-pad emissions by production cohort to those based on our grid-level normalization approach. To do this, we simulate emissions for individual well-pads and measure the difference in the emissions proportions at various production cohorts between the normalized gridded values and simulated well-pad data. Additional detail on these sensitivity tests is presented in the SI – Section 1.

**National estimates of production sector oil/gas emissions**

We estimate production-related methane emissions to the contiguous U.S. constrained by MethaneSAT data by leveraging the wells-only grid cells and the inverse relationship between methane intensity and oil/gas production (Fig. S6) (Eq. 2), where $I_i$ is the oil/gas methane intensity in $\log_{10}$ format for wells-only grid cell $i$, $\beta_0$ is the intercept, $\beta_1$ is the slope of the trendline, $P_i$ is the total oil/gas production in $\log_{10}$ scale associated with wells-only grid cell $i$, $\varepsilon_i$

is the residual error. (1) We isolate all wells-only grid cells from the MethaneSAT observation domains with non-zero well-pad emissions estimates and calculate the associated slope relating the log-scale oil/gas production and energy intensity. We use energy intensity rather than loss rates to better capture regions with significant oil production.

$$I_i = \beta_0 + \beta_1 P_i + \varepsilon_i \tag{2}$$

(2) We bin all wells-only grid cells into five groups assigned according to grid cell production, with the production ranges being <2 boe $d^{-1}$, 2-15 boe $d^{-1}$, 15-100 boe $d^{-1}$, 100-1,000 boe $d^{-1}$, and >1,000 boe $d^{-1}$. (3) Using the binned data, we calculate the percentage of grid cells containing zero estimated well-pad methane emissions (Fig. S6). (4) We map the entire population of U.S. production well-pads onto a $4 \times 4$ $km^2$ grid and aggregate oil/gas production by grid cell. (5) Using the grid-level production estimates, we calculate an associated energy intensity informed from our linear model and resample from the residual error to assign an energy intensity value to each grid cell. (6) According to the production level for each grid cell, we randomly assign the grid cell as “non-emitting” based on the probability calculated in (3), where a non-emitting grid cell is assigned an oil and gas methane emission rate of 0 kg $h^{-1}$. (7) We calculate the associated methane emissions for the grid cell based on the assigned intensity value, unless the grid cell is classified as non-emitting. Using this measurement-constrained approach, we estimate production-related methane emissions for all areas that were not observed by the satellite-based measurements, and areas that were observed but contain a mixture of production well-pads and other oil and gas infrastructure.

## REFERENCES


1. Y. Shan, K. Tian, R. Li, Y. Guan, J. Ou, D. Guan, K. Hubacek, Global methane footprints growth and drivers 1990-2023. *Nat Commun* **16**, 8184 (2025).

2. J. E. Aldy, F. L. Reinhardt, R. N. Stavins, Methane Abatement Costs in the Oil and Gas Industry: Survey and Synthesis. National Bureau of Economic Research 33564 [Preprint] (2025). https://doi.org/10.3386/w33564.

3. D. Shindell, A. R. Ravishankara, J. C. I. Kuylenstierna, E. Michalopoulou, L. Höglund-Isaksson, Y. Zhang, K. Seltzer, M. Ru, R. Castelino, G. Faluvegi, V. Naik, L. Horowitz, J. He, J.-F. Lamarque, K. Sudo, W. J. Collins, C. Malley, M. Harmsen, K. Stark, J. Junkin, G. Li, A. Glick, N. Borgford-Parnell, Global Methane Assessment: Benefits and Costs of Mitigating Methane Emissions (2021). https://ntrs.nasa.gov/citations/20210015658.

4. J. D. East, D. J. Jacob, D. Jervis, N. Balasus, L. A. Estrada, S. E. Hancock, M. P. Sulprizio, J. Thomas, X. Wang, Z. Chen, D. J. Varon, J. R. Worden, Worldwide inference of national methane emissions by inversion of satellite observations with UNFCCC prior estimates. *Nat Commun* **16**, 11004 (2025).

5. L. Shen, D. J. Jacob, R. Gautam, M. Omara, T. R. Scarpelli, A. Lorente, D. Zavala-Araiza, X. Lu, Z. Chen, J. Lin, National quantifications of methane emissions from fuel exploitation using high resolution inversions of satellite observations. *Nat Commun* **14**, 4948 (2023).

6. D. Jervis, M. Girard, J.-P. W. MacLean, D. Marshall, J. McKeever, M. Strupler, A. Ramier, E. Tarrant, D. Young, J. D. Maasakkers, I. Aben, T. R. Scarpelli, Global energy sector methane emissions estimated by using facility-level satellite observations. *Science* **390**, 1151–1155 (2025).

7. R. Duren, D. Cusworth, A. Ayasse, K. Howell, A. Diamond, T. Scarpelli, J. Kim, K. O’neill, J. Lai-Norling, A. Thorpe, S. R. Zandbergen, L. Shaw, M. Keremedjiev, J. Guido, P. Giuliano, M. Goldstein, R. Nallapu, G. Barentsen, D. R. Thompson, K. Roth, D. Jensen, M. Eastwood, F. Reuland, T. Adams, A. Brandt, E. A. Kort, J.

Mason, R. O. Green, The Carbon Mapper emissions monitoring system. *Atmospheric Measurement Techniques* **18**, 6933–6958 (2025).

8. J. P. Williams, J. Benmergui, M. Knapp, M. Omara, A. Himmelberger, E. Kyzivat, K. Weatherby, B. Lyke, J. Warren, K. MacKay, S. Ayvazov, M. Russi, N. LoFaso, T. Melendez, C. C. Miller, S. Roche, M. Sargent, J. Franklin, M. Nasr, Z. Zhang, D. Miller, B. Luo, L. Guanter, S. P. Hamburg, S. C. Wofsy, R. Gautam, Methane intensity and emissions across major oil and gas basins and individual jurisdictions using MethaneSAT observations. *EGUsphere*, 1–30 (2025).

9. C. Chan Miller, S. Roche, J. S. Wilzewski, X. Liu, K. Chance, A. H. Souri, E. Conway, B. Luo, J. Samra, J. Hawthorne, K. Sun, C. Staebell, A. Chulakadabba, M. Sargent, J. S. Benmergui, J. E. Franklin, B. C. Daube, Y. Li, J. L. Laughner, B. C. Baier, R. Gautam, M. Omara, S. C. Wofsy, Methane retrieval from MethaneAIR using the $CO_2$ proxy approach: a demonstration for the upcoming MethaneSAT mission. *Atmospheric Measurement Techniques* **17**, 5429–5454 (2024).

10. C. Chan Miller, S. Roche, J. Wilzweski, X. Liu, K. V. Chance, B. Luo, K. Sun, J. E. Franklin, J. S. Benmergui, M. Nasr, D. J. Miller, S. Crowell, N. Leisso, E. Walker, R. Gautam, N. LoFaso, S. Ayvazov, D. Wells, C. Cervantes, C. Hairfield, S. Wofsy, Operational $XCH_4$ Retrievals from MethaneSAT: Demonstrating Sensor Performance for Constraining Regional Methane Emissions. *EGUsphere*, 1–40 (2026).

11. M. Crippa, D. Guizzardi, F. Pagani, M. Schiavina, M. Melchiorri, E. Pisoni, F. Graziosi, M. Muntean, J. Maes, L. Dijkstra, M. Van Damme, L. Clarisse, P. Coheur, Insights into the spatial distribution of global, national, and subnational greenhouse gas emissions in the Emissions Database for Global Atmospheric Research (EDGAR v8.0). *Earth System Science Data* **16**, 2811–2830 (2024).

12. T. R. Scarpelli, E. Roy, D. J. Jacob, M. P. Sulprizio, R. D. Tate, D. H. Cusworth, Using new geospatial data and 2020 fossil fuel methane emissions for the Global Fuel Exploitation Inventory (GFEI) v3. *Earth System Science Data* **17**, 7019–7033 (2025).

13. J. D. Maasakkers, E. E. McDuffie, M. P. Sulprizio, C. Chen, M. Schultz, L. Brunelle, R. Thrush, J. Steller, C. Sherry, D. J. Jacob, S. Jeong, B. Irving, M. Weitz, A Gridded Inventory of Annual 2012–2018 U.S. Anthropogenic Methane Emissions. *Environ. Sci. Technol.* **57**, 16276–16288 (2023).

14. C. Granier, S. Darras, H. Denier van Der Gon, D. Jana, N. Elguindi, G. Bo, G. Michael, G. Marc, J.-P. Jalkanen, J. Kuenen, C. Liousse, B. Quack, D. Simpson, K. Sindelarova, "The Copernicus Atmosphere Monitoring Service global and regional emissions (April 2019 version)" (Research Report, Copernicus Atmosphere Monitoring Service, 2019); https://doi.org/10.24380/d0bn-kx16.

15. ogcidev, Methane intensity target - OGCI (2023). https://www.ogci.com/methane-emissions/methane-intensity-target/.

16. OGDC - The Charter, *OGDC*. https://www.ogdc.org/.

17. D. J. Varon, D. J. Jacob, L. A. Estrada, N. Balasus, J. D. East, D. C. Pendergrass, Z. Chen, M. Sulprizio, M. Omara, R. Gautam, Z. R. Barkley, F. J. C. Saldaña, E. K. Reidy, H. Kamdar, E. D. Sherwin, S. C. Biraud, D. Jervis, S. Pandey, J. R. Worden, K. W. Bowman, J. D. Maasakkers, R. L. Kleinberg, Seasonality and Declining Intensity of Methane Emissions from the Permian and Nearby US Oil and Gas Basins. *Environ. Sci. Technol.* **60**, 425–435 (2026).

18. J. P. Veefkind, R. Serrano-Calvo, J. de Gouw, B. Dix, O. Schneising, M. Buchwitz, J. Barré, R. J. van der A, M. Liu, P. F. Levelt, Widespread Frequent Methane Emissions From the Oil and Gas Industry in the Permian Basin. *Journal of Geophysical Research: Atmospheres* **128**, e2022JD037479 (2023).

19. D. J. Varon, D. J. Jacob, B. Hmiel, R. Gautam, D. R. Lyon, M. Omara, M. Sulprizio, L. Shen, D. Pendergrass, H. Nesser, Z. Qu, Z. R. Barkley, N. L. Miles, S. J. Richardson, K. J. Davis, S. Pandey, X. Lu, A. Lorente, T. Borsdorff, J. D. Maasakkers, I. Aben, Continuous weekly monitoring of methane emissions from the Permian Basin by inversion of TROPOMI satellite observations. *Atmospheric Chemistry and Physics* **23**, 7503–7520 (2023).

20. M. Omara, D. Zavala-Araiza, D. R. Lyon, B. Hmiel, K. A. Roberts, S. P. Hamburg, Methane emissions from US low production oil and natural gas well sites. *Nat Commun* **13**, 2085 (2022).

21. R. L. Bowers, "Quantification of Methane Emissions from Marginal (Low Production Rate) Oil and Natural Gas Wells" (DOE-GSI-31702, GSI Environmental Inc., Austin, TX (United States), 2022); https://doi.org/10.2172/1865859.

22. J. A. Deighton, A. Townsend-Small, S. J. Sturmer, J. Hoschouer, L. Heldman, Measurements show that marginal wells are a disproportionate source of methane relative to production. *Journal of the Air & Waste Management Association* **70**, 1030–1042 (2020).

23. M. Omara, A. Himmelberger, K. MacKay, J. P. Williams, J. Benmergui, M. Sargent, S. C. Wofsy, R. Gautam, Constructing a measurement-based spatially explicit inventory of US oil and gas methane emissions (2021). *Earth System Science Data* **16**, 3973–3991 (2024).

24. J. P. Williams, M. Omara, A. Himmelberger, D. Zavala-Araiza, K. MacKay, J. Benmergui, M. Sargent, S. C. Wofsy, S. P. Hamburg, R. Gautam, Small emission sources in aggregate disproportionately account for a large majority of total methane emissions from the US oil and gas sector. *Atmospheric Chemistry and Physics* **25**, 1513–1532 (2025).

25. K. MacKay, J. Benmergui, J. P. Williams, M. Omara, A. Himmelberger, M. Sargent, J. D. Warren, C. C. Miller, S. Roche, Z. Zhang, L. Guanter, S. Wofsy, R. Gautam, Assessment of methane emissions from US onshore oil and gas production using MethaneAIR measurements. *EGUsphere*, 1–24 (2025).

26. Wood Mackenzie (2021). https://www.woodmac.com/lens.

27. R. A. Alvarez, D. Zavala-Araiza, D. R. Lyon, D. T. Allen, Z. R. Barkley, A. R. Brandt, K. J. Davis, S. C. Herndon, D. J. Jacob, A. Karion, E. A. Kort, B. K. Lamb, T. Lauvaux, J. D. Maasakkers, A. J. Marchese, M. Omara, S. W. Pacala, J. Peischl, A. L. Robinson, P. B. Shepson, C. Sweeney, A. Townsend-Small, S. C. Wofsy, S. P. Hamburg, Assessment of methane emissions from the U.S. oil and gas supply chain. *Science* **361**, 186–188 (2018).

28. D. H. Cusworth, A. K. Thorpe, A. K. Ayasse, D. Stepp, J. Heckler, G. P. Asner, C. E. Miller, V. Yadav, J. W. Chapman, M. L. Eastwood, R. O. Green, B. Hmiel, D. R. Lyon, R. M. Duren, Strong methane point sources contribute a disproportionate fraction of total emissions across multiple basins in the United States. *Proceedings of the National Academy of Sciences* **119**, e2202338119 (2022).

29. S. Seymour, D. Xie, M. Kang, S. Schwietzke, D. Zavala-Araiza, S. Hamburg, Methane emission intensity metrics: unmasking the trade-offs. (2025).

30. M. R. Johnson, B. Conrad, D. J. Zimmerle, R. L. Kleinberg, Methane by the Numbers: The Need for Clear and Comparable Methane Intensity Metrics. (2025).

31. Z. R. Barkley, T. Lauvaux, K. J. Davis, A. Deng, N. L. Miles, S. J. Richardson, Y. Cao, C. Sweeney, A. Karion, M. Smith, E. A. Kort, S. Schwietzke, T. Murphy, G. Cervone, D. Martins, J. D. Maasakkers, Quantifying methane emissions from natural gas production in north-eastern Pennsylvania. *Atmospheric Chemistry and Physics* **17**, 13941–13966 (2017).

32. J. Peischl, T. B. Ryerson, K. C. Aikin, J. A. de Gouw, J. B. Gilman, J. S. Holloway, B. M. Lerner, R. Nadkarni, J. A. Neuman, J. B. Nowak, M. Trainer, C. Warneke, D. D. Parrish, Quantifying atmospheric methane emissions from the Haynesville, Fayetteville, and northeastern Marcellus shale gas production regions. *Journal of Geophysical Research: Atmospheres* **120**, 2119–2139 (2015).

33. M. Omara, N. Zimmerman, M. R. Sullivan, X. Li, A. Ellis, R. Cesa, R. Subramanian, A. A. Presto, A. L. Robinson, Methane Emissions from Natural Gas Production Sites in the United States: Data Synthesis and National Estimate. *Environ. Sci. Technol.* **52**, 12915–12925 (2018).

34. M. Omara, R. Gautam, M. A. O'Brien, A. Himmelberger, A. Franco, K. Meisenhelder, G. Hauser, D. R. Lyon, A. Chulakadabba, C. C. Miller, J. Franklin, S. C. Wofsy, S. P. Hamburg, Developing a spatially explicit global

oil and gas infrastructure database for characterizing methane emission sources at high resolution. *Earth System Science Data* **15**, 3761–3790 (2023).

35. Enverus | Creating the future of energy together. (2024). https://www.enverus.com/.

36. M. Saunois, A. Martinez, B. Poulter, Z. Zhang, P. A. Raymond, P. Regnier, J. G. Canadell, R. B. Jackson, P. K. Patra, P. Bousquet, P. Ciais, E. J. Dlugokencky, X. Lan, G. H. Allen, D. Bastviken, D. J. Beerling, D. A. Belikov, D. R. Blake, S. Castaldi, M. Crippa, B. R. Deemer, F. Dennison, G. Etiope, N. Gedney, L. Höglund-Isaksson, M. A. Holgerson, P. O. Hopcroft, G. Hugelius, A. Ito, A. K. Jain, R. Janardanan, M. S. Johnson, T. Kleinen, P. B. Krummel, R. Lauerwald, T. Li, X. Liu, K. C. McDonald, J. R. Melton, J. Mühle, J. Müller, F. Murguia-Flores, Y. Niwa, S. Noce, S. Pan, R. J. Parker, C. Peng, M. Ramonet, W. J. Riley, G. Rocher-Ros, J. A. Rosentreter, M. Sasakawa, A. Segers, S. J. Smith, E. H. Stanley, J. Thanwerdas, H. Tian, A. Tsuruta, F. N. Tubiello, T. S. Weber, G. R. van der Werf, D. E. J. Worthy, Y. Xi, Y. Yoshida, W. Zhang, B. Zheng, Q. Zhu, Q. Zhu, Q. Zhuang, Global Methane Budget 2000–2020. *Earth System Science Data* **17**, 1873–1958 (2025).

37. US Oil and Gas Wells by Production Rate - U.S. Energy Information Administration (EIA). https://www.eia.gov/petroleum/wells/index.php.

38. D. W. S. Wong, "The Modifiable Areal Unit Problem (MAUP)" in *WorldMinds: Geographical Perspectives on 100 Problems*, D. G. Janelle, B. Warf, K. Hansen, Eds. (Springer Netherlands, Dordrecht, 2004; http://link.springer.com/10.1007/978-1-4020-2352-1_93), pp. 571–575.

39. C. A. Gotway, L. J. Young, Combining Incompatible Spatial Data. *Journal of the American Statistical Association* **97**, 632–648 (2002).

40. C. P. Donahue, K. Oberoi, J. W. Dillon, V. Hengst, B. Kennedy, W. Kearney, J. Lennox, E. Rehbein, R. Sykes, C. D. Dudiak, D. T. Altamura, G. Doherty, P. A. Roos, J. K. Brasseur, M. J. Thorpe, Aerial LiDAR-Based, Source-Resolved Methane Emissions Inventory: Permian Basin Case Study for Benchmarking U.S. Emissions. *Environ. Sci. Technol.* **60**, 13968–13979 (2026).

41. Appalachian Methane Initiative (AMI), *CEESA*. https://www.ceesa.utexas.edu/ami.

42. C. P. Donahue, K. Oberoi, J. Dillon, V. Hengst, B. Kennedy, W. Kearney, J. Lennox, E. Rehbein, R. Sykes, C. Dudiak, D. Altamura, G. Doherty, P. Roos, J. K. Brasseur, M. Thorpe, Aerial LiDAR Based, Source Resolved Methane Emissions Inventory: Permian Basin Case Study for Benchmarking U.S. Emissions. (2025).

43. R. Duren, D. Cusworth, A. Ayasse, K. Howell, A. Diamond, T. Scarpelli, J. Kim, K. O'neill, J. Lai-Norling, A. Thorpe, S. R. Zandbergen, L. Shaw, M. Keremedjiev, J. Guido, P. Giuliano, M. Goldstein, R. Nallapu, G. Barentsen, D. R. Thompson, K. Roth, D. Jensen, M. Eastwood, F. Reuland, T. Adams, A. Brandt, E. A. Kort, J. Mason, R. O. Green, The Carbon Mapper emissions monitoring system. *Atmospheric Measurement Techniques* **18**, 6933–6958 (2025).

44. L. Guanter, J. Roger, J. Warren, M. Sargent, Z. Zhang, S. Roche, C. C. Miller, M. Steiner, H. Hadfield, M. Omara, J. Williams, K. MacKay, J. E. Franklin, B. Luo, S. C. Wofsy, S. P. Hamburg, R. Gautam, Surveying methane point-source super-emissions across oil and gas basins with MethaneSAT. *Atmospheric Chemistry and Physics* **26**, 2941–2963 (2026).

45. The MethaneSAT Science and Engineering Team, MethaneSAT Level-4 Dispersed Emissions Product: Algorithm Theoretical Basis Document v1.1. doi: 10.5281/zenodo.19873046 (2026).

46. J. P. Williams, J. Benmergui, M. Knapp, M. Omara, A. Himmelberger, E. Kyzivat, K. Weatherby, B. Lyke, J. Warren, K. MacKay, S. Ayvazov, M. Russi, N. LoFaso, T. Melendez, C. C. Miller, S. Roche, M. Sargent, J. Franklin, M. Nasr, Z. Zhang, D. J. Miller, B. Luo, L. Guanter, S. P. Hamburg, S. C. Wofsy, R. Gautam, Methane intensity and emissions across major oil and gas basins and individual jurisdictions using MethaneSAT observations. *Atmospheric Chemistry and Physics* **26**, 5961–5981 (2026).

47. B. Fasoli, J. C. Lin, D. R. Bowling, L. Mitchell, D. Mendoza, Simulating atmospheric tracer concentrations for spatially distributed receptors: updates to the Stochastic Time-Inverted Lagrangian Transport model's R interface (STILT-R version 2). *Geoscientific Model Development* **11**, 2813–2824 (2018).

48. J. C. Lin, C. Gerbig, S. C. Wofsy, A. E. Andrews, B. C. Daube, K. J. Davis, C. A. Grainger, A near-field tool for simulating the upstream influence of atmospheric observations: The Stochastic Time-Inverted Lagrangian Transport (STILT) model. *Journal of Geophysical Research: Atmospheres* **108** (2003).

49. NOAA Institutional Repository. https://repository.library.noaa.gov.

50. M. D. Hoffman, A. Gelman, The No-U-Turn Sampler: Adaptively Setting Path Lengths in Hamiltonian Monte Carlo. arXiv arXiv:1111.4246 [Preprint] (2011). https://doi.org/10.48550/arXiv.1111.4246.

51. B. Carpenter, A. Gelman, M. D. Hoffman, D. Lee, B. Goodrich, M. Betancourt, M. Brubaker, J. Guo, P. Li, A. Riddell, Stan: A Probabilistic Programming Language. *Journal of Statistical Software* **76**, 1–32 (2017).

52. M. Omara, A. Himmelberger, K. MacKay, J. P. Williams, J. Benmergui, M. Sargent, S. C. Wofsy, R. Gautam, Constructing a measurement-based spatially explicit inventory of US oil and gas methane emissions (2021). *Earth System Science Data* **16**, 3973–3991 (2024).

53. A. A. Bloom, K. W. Bowman, M. Lee, A. J. Turner, R. Schroeder, J. R. Worden, R. Weidner, K. C. McDonald, D. J. Jacob, A global wetland methane emissions and uncertainty dataset for atmospheric chemical transport models (WetCHARTs version 1.0). *Geoscientific Model Development* **10**, 2141–2156 (2017).

54. D. C. Pendergrass, D. J. Jacob, N. Balasus, L. Estrada, D. J. Varon, J. D. East, M. He, T. A. Mooring, E. Penn, H. Nesser, J. R. Worden, Trends and seasonality of 2019–2023 global methane emissions inferred from a localized ensemble transform Kalman filter (CHEEREIO v1.3.1) applied to TROPOMI satellite observations. *Atmospheric Chemistry and Physics* **25**, 14353–14369 (2025).

55. Z. R. Barkley, K. J. Davis, N. L. Miles, S. J. Richardson, Examining Daily Temporal Characteristics of Oil and Gas Methane Emissions in the Delaware Basin Using Continuous Tower Observations. *Journal of Geophysical Research: Atmospheres* **130**, e2024JD042050 (2025).

56. Oil & Gas Decarbonization Charter, *OGDC*. https://www.ogdc.org/oil-gas-decarbonization-charter/.

57. Overview – Global Methane Tracker 2022 – Analysis, *IEA*. http://www.iea.org/reports/global-methane-tracker-2022/overview.

58. P. M. Burdeau, E. D. Sherwin, S. C. Biraud, E. S. F. Berman, A. R. Brandt, High-resolution national mapping of natural gas composition substantially updates methane leakage impacts. *Nat Commun* **16**, 11297 (2025).

## Acknowledgments

We thank the MethaneSAT mission operations team, data processing team, and science team for the provision of data products used in this study. We acknowledge the use of publicly available emissions datasets and analysis tools that made this work possible, including products from the Copernicus Atmosphere Monitoring Service (CAMS), the Emissions Database for Global Atmospheric Research (EDGAR), Carbon Mapper, and the Global Fuel Exploitation Inventory (GFEI v3). We further acknowledge the use of open-access satellite-based methane studies that informed and supported this analysis.

**Funding:** Funding for MethaneSAT activities was provided in part by anonymous donors, Arnold Ventures, The Audacious Project, the Ballmer Group, the Bezos Earth Fund, The Children's Investment Fund Foundation, the Heising–Simons Family Fund, King Philanthropies, the Robertson Foundation, the Skyline Foundation, and the Valhalla Foundation. For a more complete list of funders, please visit https://www.methanesat.org/ (last access: 3 Aug 2026).

**Author contributions:**

Conceptualization: J.P.W., R.G.

Methodology: J.P.W., R.G., J.B., M.O., M.K.
Investigation: J.B., M.K., M.O., A.H., K.W., B.L., S.C.W., S.H.,
Visualization: J.P.W., A.H., R.G., S.H., L.G., K.M.
Supervision: R.G., S.C.W., S.H.
Writing—original draft: J.P.W., R.G.
Writing—review & editing: All authors

**Competing interests:** The authors declare they have no competing interests.

**Data, code, and materials availability:** MethaneSAT data products are publicly accessible through Google Earth Engine and Google Cloud: https://developers.google.com/earth-engine/datasets/publisher/edf-methanesat-ee. R-Studio (v. 2025.09.1) and Python code used for data analysis and visualization are available from the authors upon reasonable request.

## Supplementary Materials

A Supplementary Information document is available and contains 19 Supplementary Figures, 6 Supplementary Tables, and two written sections.

# Supplementary Materials for

## Methane emissions intensity mapping from space reveals outsized emissions impact from marginal oil and gas production in the U.S.

James P. Williams *et al.*

*Corresponding author. Email: jamwilliams@edf.org

**This PDF file includes:**

## Supplementary Text

### Estimating well-pad emissions from an area-based normalization approach

Area-based normalization of emissions to grid cells is subject to a well-documented statistical artifact known as the change-of-support problem: aggregating point-level (i.e., well-pad) values into areal units with normalized values systematically smooths out the variance present in the underlying point data (*1*, *2*). Because methane emission intensity scales non-linearly and inversely with production, with marginal well-pads contributing disproportionately large emissions relative to their output, this smoothing is expected to bias grid-level, production-normalized emissions estimates toward underestimating the true proportion of emissions attributable to marginal well-pads. Furthermore, a production-normalized cutoff value of <15 boe $d^{-1}$ well-pad$^{-1}$ effectively constrains the production of non-marginal well-pads within marginally-producing areas, whereas there is no constraint on the production of non-marginal well-pads within non-marginally producing areas. This discrepancy is evident in the average production of non-marginally producing well-pads within marginally-producing areas at 29 boe $d^{-1}$ well-pad$^{-1}$ compared to 320 boe $d^{-1}$ well-pad$^{-1}$ in non-marginally producing areas (Table S6). This leads to a redistribution of emissions driven mostly by site counts rather than production levels, with ~91,000 marginal well-pads within non-marginal areas and ~22,000 non-marginal well-pads within marginal areas (Table S6; SI – Section 1).

To assess the magnitude of the change-of-support effect and recover a more accurate estimate of true well-pad-level emissions contributions, we perform two sensitivity tests. First, we conduct a series of simulations to test the impacts of the grid-level aggregation to produce our well-normalized production metrics across the full population of CONUS well-pads. Second, we estimate the total emissions contribution of marginal well-pad emissions within non-marginal areas, and of non-marginal well-pads within marginal areas, and redistribute their emissions to their respective production cohort. For the simulation tests, we utilize the actual population of well-pads within the CONUS and their associated production, then assign emission rates to those well-pads from the log/log relationship between oil and gas methane intensity and production (Eq. 1; Eq. 2), where $I_i$ is the oil/gas methane intensity for well-pad $i$, $\beta_0$ is the intercept, $\beta_1$ is the slope of the trendline, $P_i$ is the production associated with well-pad $i$, $\varepsilon_i$ is the residual error, and Ei is the methane emissions from well-pad $i$.

Eq. 1: $$I_i = \beta_0 + \beta_1 P_i + \varepsilon_i$$

Eq. 2: $$E_i = I_i P_i$$

Like our area-based production normalization approach we use in the main paper, we aggregate both the simulated emissions and production from the well-pads to a grid and calculate the differences between the estimated emissions contributions by production class using both the true well-pad production, and the well-pad normalized production metrics. For the second sensitivity test, we average the total well-pad level production of marginal well-pads within non-marginal areas, and vice versa (Table S6). Next, we take wells-only emissions data from MethaneSAT for grid cells that contain only one well-pad and estimate linear model parameters on the energy intensity versus oil and gas production (Fig. S14a). Using this relationship, and the average production from the well-pads, we estimate a corresponding energy intensity which is in turn converted to cumulative methane emissions for the well-pads of interest. We then re-distribute emissions from non-marginal well-pads in marginal areas to non-marginal areas, and vice versa, to estimate the proportion of marginal/non-marginal well-pad emissions relative to the total well-pad emissions.

We perform a series of 3,125 simulations that examine the impacts of three different factors that on the relationship between production and emissions. The purpose of this first suite of simulations is to determine which factor exerts the strongest influence on the differences between well-pad and aggregated grid-level production and emissions. The three factors we test in this first round of simulations are the size of the grid cells used to aggregate the simulated well-pad emissions and production, the slope of the intensity versus production relationship, and the intercept of the intensity versus production relationship. All the factors being tested in this first simulation step are outlined in Table S2. We summarize the results of the first round of simulations using a Random Forest regression model, which quantifies the relative importance of input parameters in explaining variation in the simulation output (ie., the absolute difference between the grid- and well-pad level proportion of emissions). Next, we perform a second set of simulations using an estimated production/intensity relationship that we assume best corresponds to the production/intensity relationship for individual well-pads, and the inversion resolution that best represents our satellite emissions data. For the second set of simulations, we assume normal distributions on the intensity/production relationship parameters and repeat 500 estimates to establish an upper and lower bound on our estimated differences between gridded and well-pad emission proportions at different production cohorts. To establish the parameters of the intensity/production relationship, we use wells-only emissions data from MethaneSAT for grid cells that contain only one well-pad (Fig. S14a), and wells-only emissions data from MethaneSAT with emissions and production normalized by well-pad counts (Fig. S14b).

Methane emissions are simulated for well-pads in the CONUS by varying parameters in the linear $\log_{10}/\log_{10}$ relationship between energy intensity and oil and gas production, with basin-level examples of simulated emissions shown in Fig. S12. Based on a Random Forest regression model, we find that the grid size has the strongest influence on the analysis of the differences between point- and grid-level aggregation of production and emissions (Table S2; Fig S13), followed by the slope of the intensity versus production relationship (Fig. S13). We found no meaningful influence from the intercept of the production/intensity relationship on the proportion of emissions below/above production cohorts between point- and grid-level emissions (Table S2; Fig. S13). Across the full population of well-pads in the CONUS, we find that the proportion of well-pad emissions below 15 boe $d^{-1}$ well-pad$^{-1}$ is consistently underestimated by the gridded production data when normalized by well-pad counts compared to the actual well-pad emissions themselves (Fig. S13d). These results underscore the usefulness of high-resolution methane emissions data to minimize differences between grid- and point-level emissions/production data.

Next, we tested how well grid-cell normalized intensity/production relationships approximate true well-pad-level relationships, using an established intensity/production relationship informed by satellite measurements and the native inversion resolution of MethaneSAT emissions data. We fit this $\log_{10}/\log_{10}$ relationship using two input datasets: (1) single well-pad grid cells only ($n = 1,088$ grid cells), and (2) all wells-only grid cells, with production and intensity normalized by well-pad count ($n = 18,650$ grid cells) (Fig. 14). Using the single-well-pad dataset, the grid-cell normalized approach underestimated the proportion of well-pad emissions below 15 boe $d^{-1}$ well-pad$^{-1}$ by 7% (95% CI: 2–12; Fig. S14b). This underestimate was larger for the smallest production cohort (<2 boe $d^{-1}$ well-pad$^{-1}$: 10%, 95% CI: 0–20) and negligible for the largest (<300 boe $d^{-1}$ well-pad$^{-1}$: 1%, 95% CI: −5–4). Using the full wells-only dataset with well-pad-normalized production and intensity, the grid-cell approach underestimated the same three thresholds by 5% (95% CI: 2–7), 7% (95% CI: 3–12), and 1% (95% CI: −1–4), respectively (Fig. S19). Because these two datasets produced similar magnitudes of underestimation, and the wells-only dataset gave the more conservative (smaller) discrepancy at the key 15 boe $d^{-1}$ threshold, we used the wells-only, well-pad-normalized results in our primary analysis as a conservative estimate of the difference between well-pad- and grid-level emissions estimates.

In a second sensitivity test, we re-estimated emissions after reassigning well-pads to their true production cohort rather than their grid-cell-averaged one. We estimate that non-marginal well-pads located in predominantly marginal areas account for 0.6 Tg $a^{-1}$ of methane emissions, while marginal well-pads located in predominantly non-marginal areas account for 1.8 Tg $a^{-1}$. Redistributing these emissions to their correct production cohorts therefore shifts a net 1.2 Tg $a^{-1}$ onto marginal well-pads (and away from non-marginal well-pads). This adjustment raises total emissions attributed to marginal well-pads to 6.2 Tg $a^{-1}$, or 65% of total well-pad emissions. This confirms that our main finding, that at least half of production-related methane emissions in the CONUS come from marginally-producing areas, holds within uncertainty even when emissions are reassigned to their actual (rather than grid-cell-averaged) well-pad production cohorts.

Sensitivity testing of the marginal versus non-marginal emissions contributions.
We assess the sensitivity of our estimates of methane emissions from marginally and non-marginally production regions through two key approaches. The first approach addresses the issue of methane emissions from marginally or non-marginally producing grid cells being indistinguishable from adjacent ones. The second approach addresses a lack of temporal representativity in our aggregated methane emissions estimates from regions that were sampled two or fewer times. Both approaches apply a spatial filtering process to the MethaneSAT emissions products and use those filtered products to re-perform the entire process of data aggregation, sectoral disaggregation, isolation of wells-only regions, and the final extrapolation of well-pad emissions to national estimates for the US.

For the first approach, we assess whether MethaneSAT observations and the CORE inversion could distinguish emissions from marginal well-pads from other sources and classify Level 4 grid cells into two distinct groups: marginal-production regions, and non-marginal production regions. We combine both groups to establish a unified estimate of negative auto-correlations between emission grid cells of interest by leveraging the 4,000 Markov chain Monte Carlo posterior samples of each emitter grid cell within the group and those of every emitter outside it. Emitter grid cells exhibiting a correlation below −0.1 with any out-of-group emitter were considered insufficiently separable for definitive source attribution and were excluded in the sensitivity analysis. We perform these grid cell exclusions at the individual scene level, and then perform the scene aggregation, sectoral disaggregation, well-pad only spatial selection, and national extrapolation analysis exactly as performed in our main text. In addition, the posterior-predicted enhancements were mapped regionally that were attributable to each group (i.e., marginal- or non-marginal areas) in order to assess their contributions to the total enhancement indicating larger contributions linked to marginal production areas to the total scene methane enhancement, relative to the contributions of non-marginal areas (Fig. S15).

For the second approach, we analyze all aggregated emissions data and isolate regions that were observed at least three times and use these restricted domains to perform our extrapolation of total national emissions from well-pads and the associated contributions from marginally- and non-marginally producing regions. If our national results are unchanged after performing these two separate tests, we assume our results regarding the contribution of marginally-producing regions to be robust.

We find our results on the relative proportions of well-pad emissions from marginal/non-marginal regions to be robust when applying both sensitivity analyses. Our first sensitivity analysis which omits grid cells that are spatially autocorrelated with adjacent grid cells results in a national estimate of marginally-producing regions to be 49% of the total well-pad emissions, almost identical to our main results. We note a sizable drop in the total well-pad emissions when applying this method, which drop from 10.3 Tg $a^{-1}$ in our original dataset to 4.6 Tg $a^{-1}$. This is caused by the removal of high-emitting pixels from the individual scenes themselves before aggregation, artificially lowering methane emissions across the entire analysis. While the drop is notable, our estimated national contribution of marginally-producing regions to total well-pad emissions are effectively unchanged. We also find that the estimated XCH4 concentrations from marginally- and non-marginally producing regions are proportionally similar across all individual scenes used in our analysis (Fig. S15). The second sensitivity test isolated regions that were observed at least three times by MethaneSAT. The resulting filtering process reduces the spatial coverage of the MethaneSAT observations from 62% of national onshore marketed oil and gas production to 40%. Using the wells-only emissions data within the reduced spatial domains, we estimate the US onshore contribution from marginally-producing regions to be 47%, closely matching the results we present in the main text. The results of these sensitivity tests indicate our main results to be robust, and unaffected by variations in the spatial coverage of observations or any artefacts within the inversion process itself that may spatially misallocate methane emissions to marginally-producing regions, or vice versa.

For our production-only analysis relating to marginal and non-marginal producing regions, there are limitations in the infrastructure data used to filter for production-only grid cells, including gaps in facility-level data and lack of inclusion of other methane-emitting oil and gas sources (e.g., abandoned oil and gas wells). Additionally, strong localized methane emissions present within the MethaneSAT scenes (i.e., high-emitting distinct point sources) may spatially manifest as smearing across the domains, which can influence the spatial allocation of emissions. Any spatial allocation issues, or other inversion artefacts, are mitigated through the incorporation of multiple scenes into aggregated emission maps and increasing the spatial extent of the observation domain. Furthermore, we perform an additional sensitivity test that recalculates our estimated national estimates of marginal and non-marginal emissions by removing grid cells exhibiting smearing behavior and find no change to our main results. Finally, we note additional uncertainties in our sectoral disaggregation of methane emissions, both in use and application of our composite methane inventory, which underpins our estimates of the spatially-explicit oil and gas contributions. Overall, we note that our focus on contiguous oil and gas methane emissions, together with the extensive sensitivity analyses as described here, do not suggest impacts to our results and conclusions.

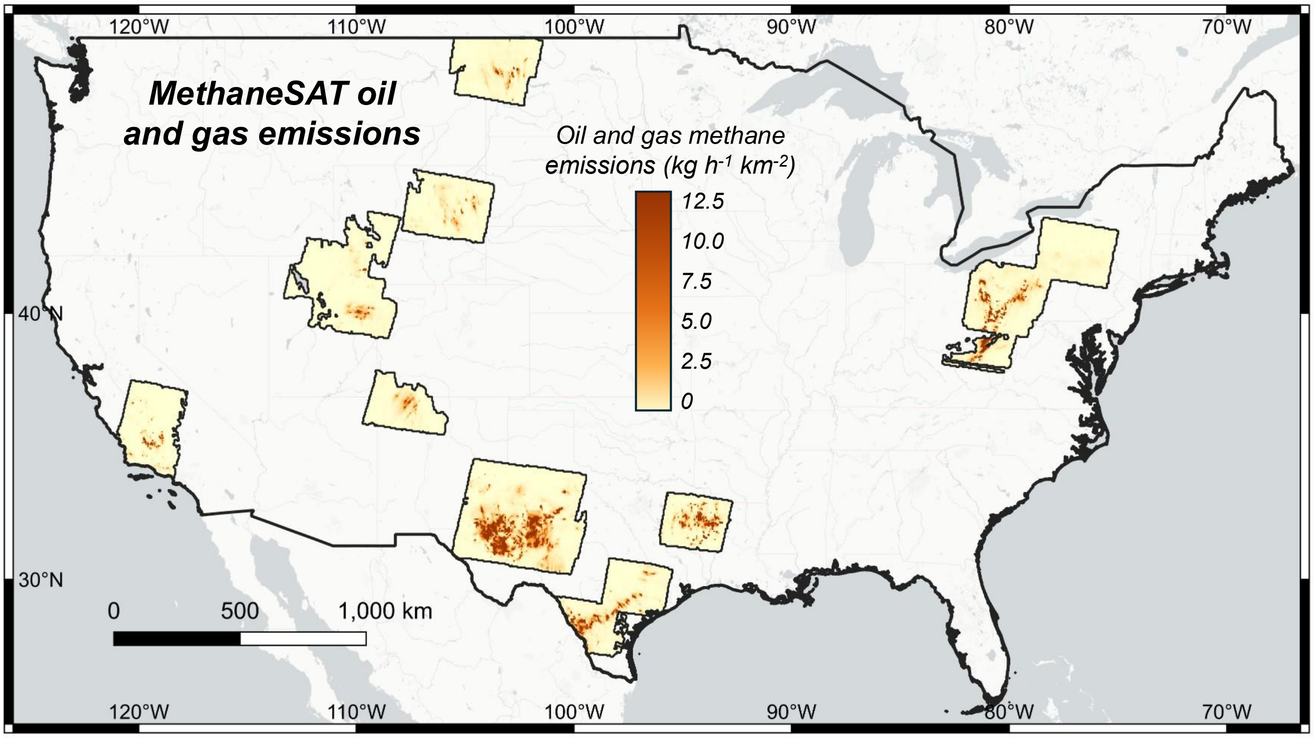


**Fig. S1.**

Map of aggregated MethaneSAT methane emissions from the oil and gas sector for the contiguous United States (CONUS). Oil and gas emissions are estimated from total methane emissions estimates from MethaneSAT L4 emissions data using the methodology described in the main text (see Methods).

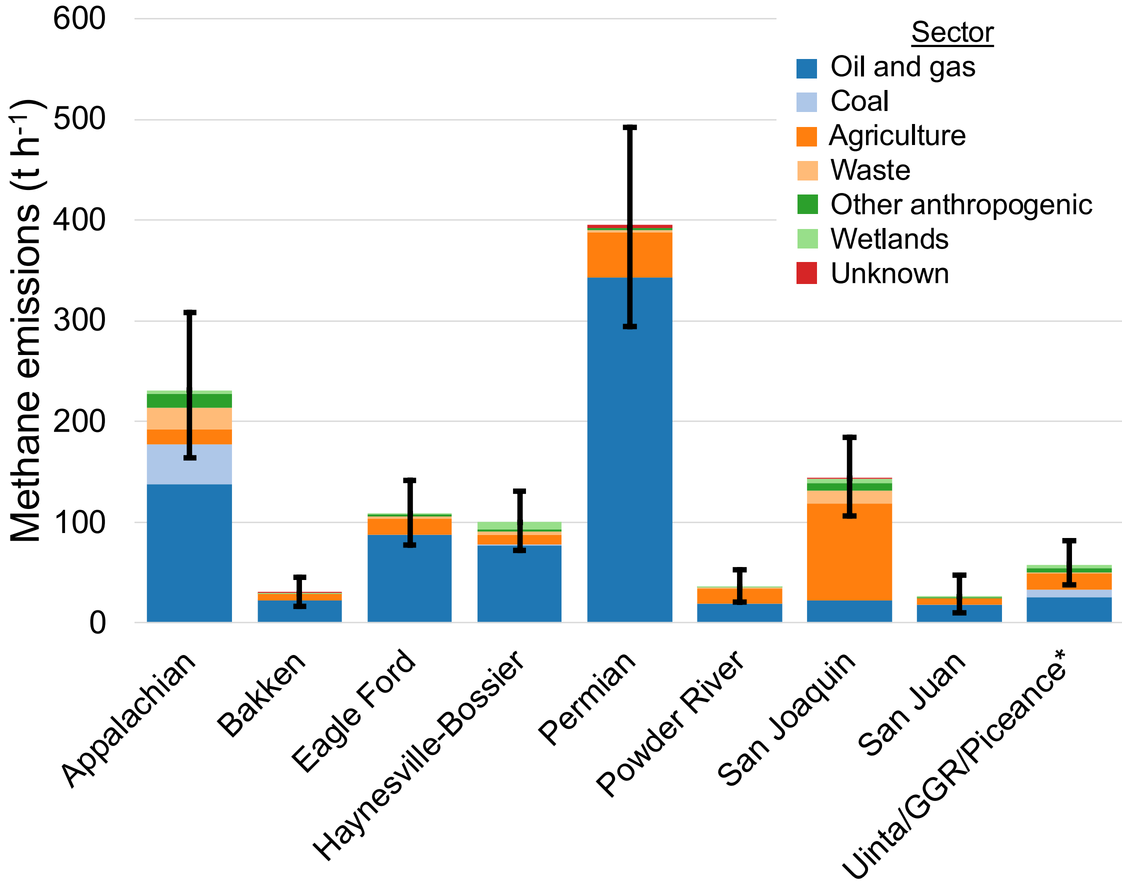


**Fig. S2.**

Sectoral breakdowns of methane emissions by observed region from MethaneSAT estimates in the contiguous United States (CONUS). The category "Other anthropogenic" includes known methane sources like wastewater treatment, post-meter distribution, transportation, chemical processing, etc. *Uinta/GGR/Piceance: Encompasses the entire observation domain by MethaneSAT over the Uinta, Greater Green River (ie., GGR), and Piceance oil and gas basins.

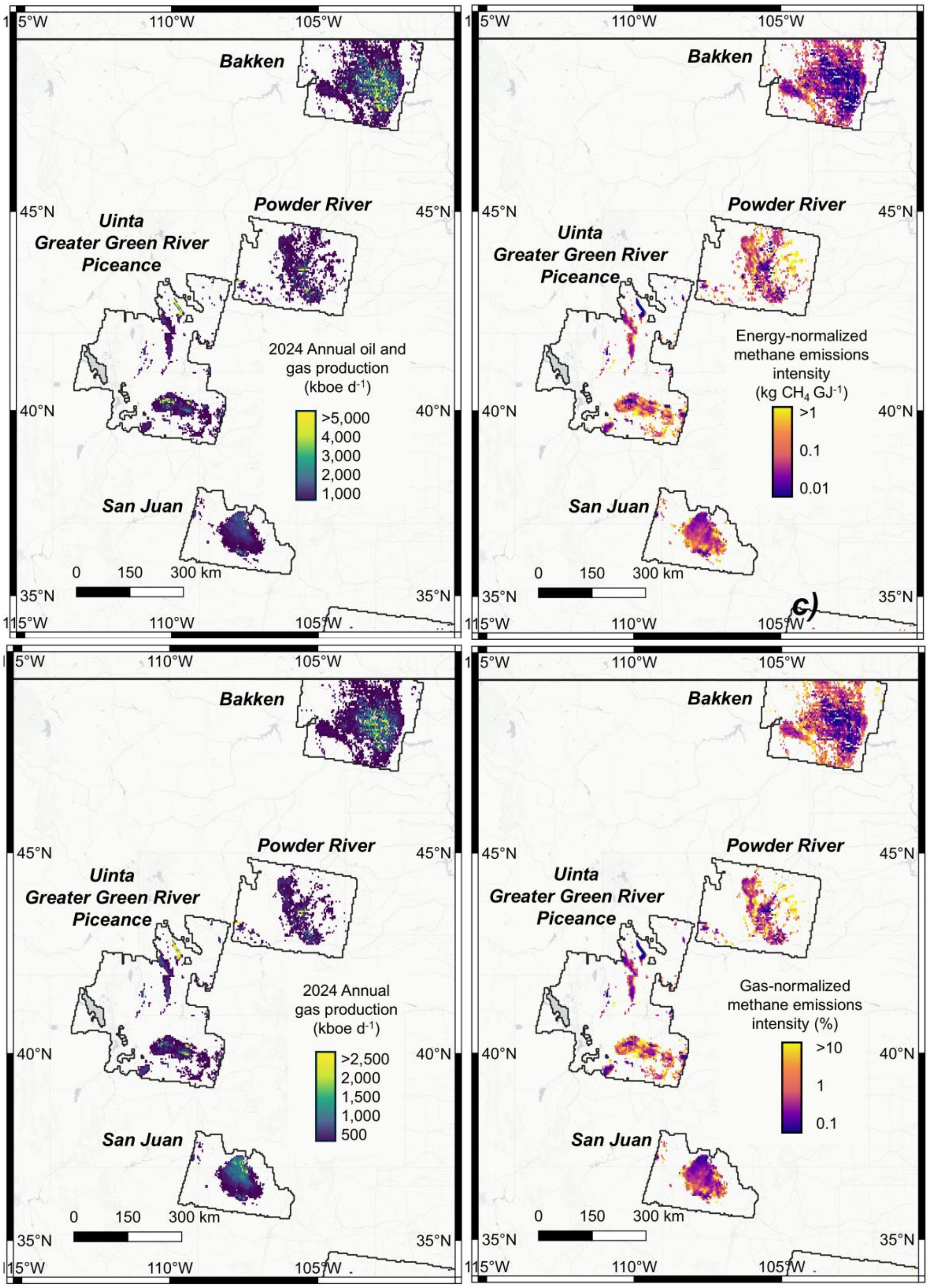


**Fig. S3.**

Maps showing aggregated MethaneSAT observation domains for the Greater Green River, Uinta, Piceance, Powder River, and San Juan oil and gas basins in the U.S. as a sample set of all covered regions in the U.S. Annual 2024 a) gas-production and c) oil and gas production gridded by MethaneSAT observation grid cells (*3*). Gridded b) gas-normalized and d) energy-normalized methane intensities at the native 4 by 4 km$^2$ grid cell resolution of MethaneSAT emissions. Note that methane emissions intensity metrics in panels b,d) are presented in $\log_{10}$ scale.

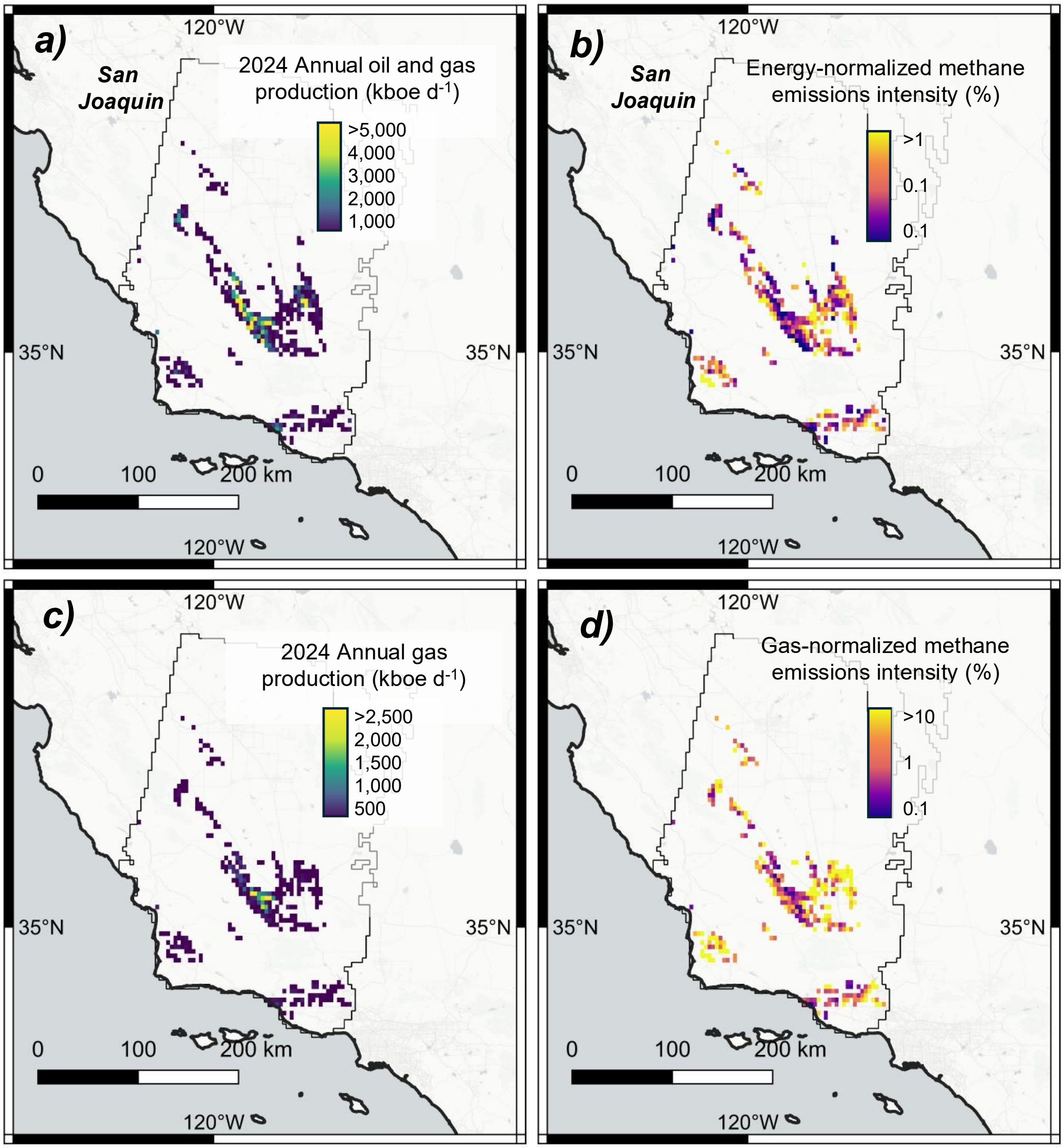


**Fig. S4.**

Maps showing aggregated MethaneSAT observation domains for the San Joaquin oil and gas basin in the U.S. as a sample set of all covered regions in the U.S. Annual 2024 a) gas-production and c) oil and gas production gridded by MethaneSAT observation grid cells (*3*). Gridded b) gas-normalized and d) energy-normalized methane intensities at the native 4 by 4 $km^2$ grid cell resolution of MethaneSAT emissions. Note that methane emissions intensity metrics in panels b,d) are presented in $\log_{10}$ scale.

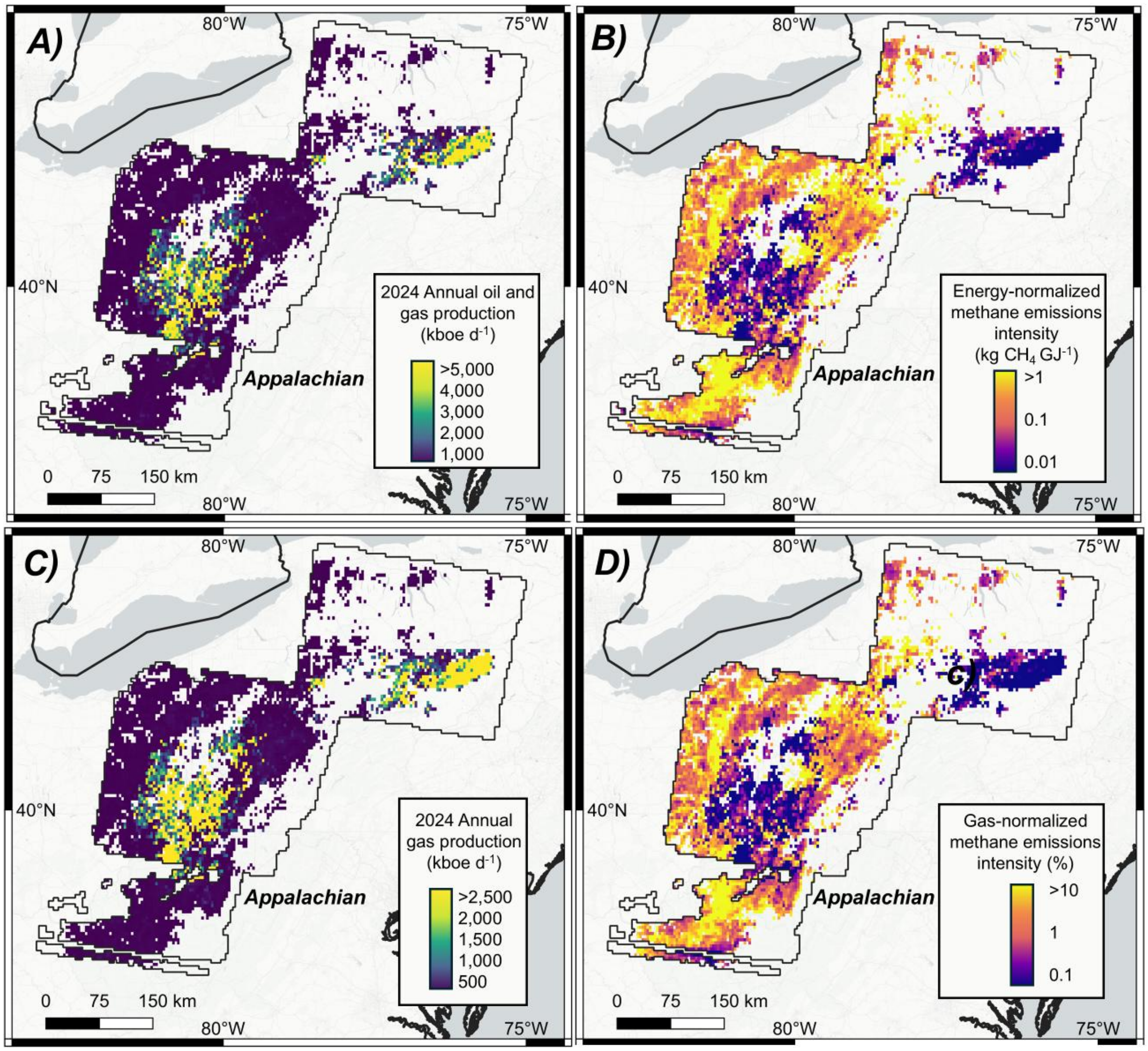


**Fig. S5.**

Maps showing aggregated MethaneSAT observation domains for the Appalachian oil and gas basin in the U.S. as a sample set of all covered regions in the U.S. Annual 2024 a) gas-production and c) oil and gas production gridded by MethaneSAT observation grid cells (*3*). Gridded b) gas-normalized and d) energy-normalized methane intensities at the native 4 by 4 $km^2$ grid cell resolution of MethaneSAT emissions. Note that methane emissions intensity metrics in panels b,d) are presented in $log_{10}$ scale.

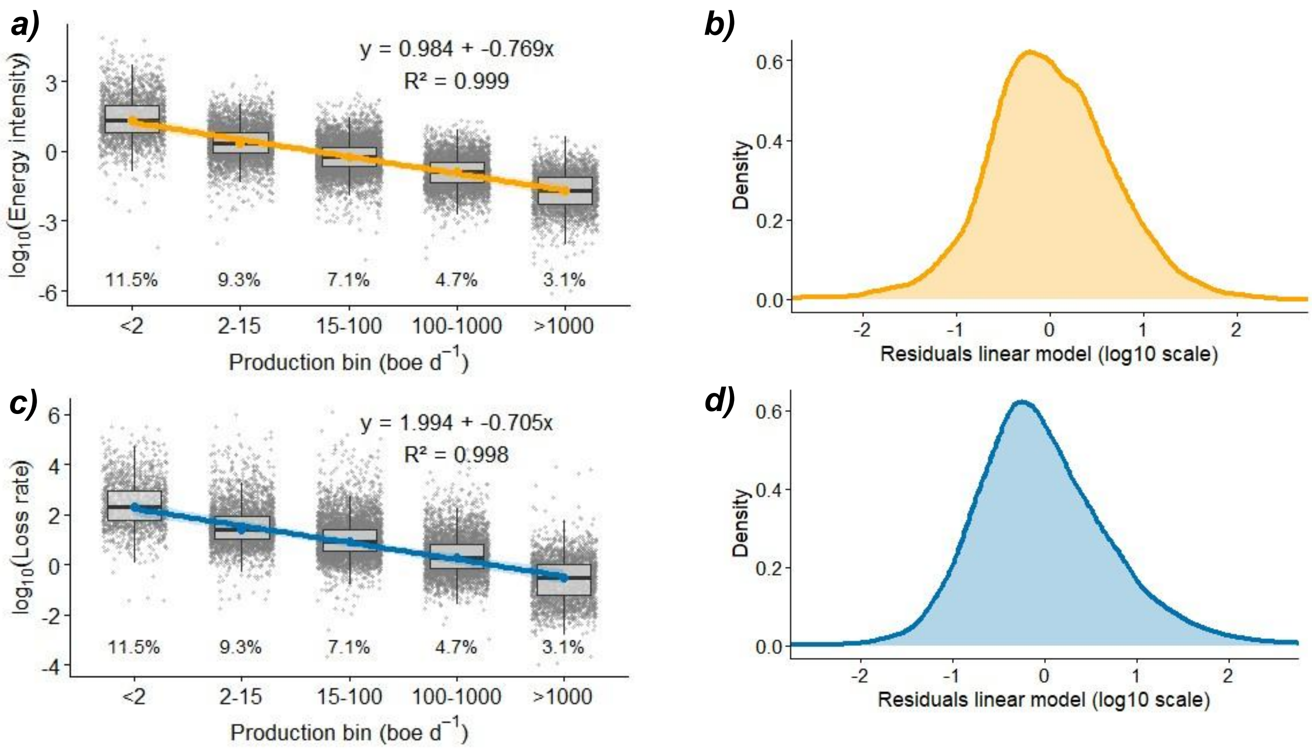


**Fig. S6.**

Boxplots of a) combined oil/gas-production normalized methane intensity (ie., energy intensity) and b) gas-normalized methane intensity (ie., loss rates) observed by MethaneSAT at the grid cell level (4 × 4 km). The percentage of grid cells within a binned production cohort with no estimated well-pad methane emissions are shown in text above the bin. Correlation coefficients and linear regression equations are displayed in the upper right of the panels corresponding to the median methane intensities by binned production cohort. Methane intensity values are calculated on a log10 scale. c,d) Kernel density plots of the residual errors (ie., predicted versus estimated methane intensity) of the model fit on un-binned data presented on a log10 scale.

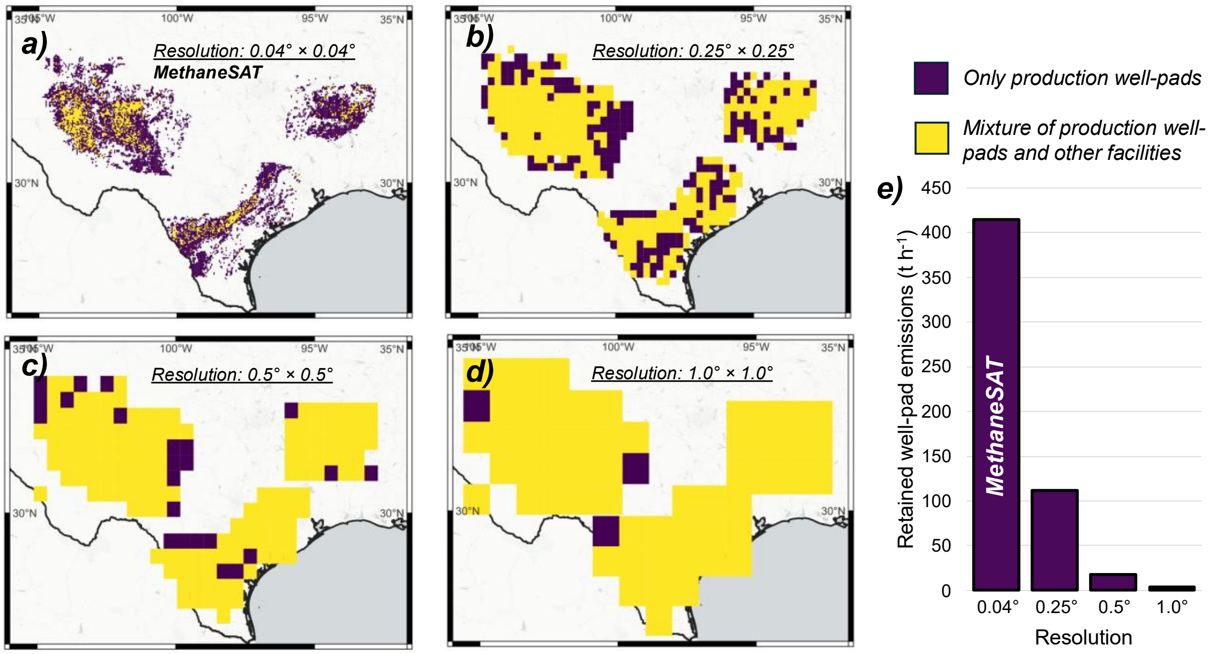


**Fig. S7.**

a,b,c,d) Maps displaying areas solely containing production well-pads versus areas that contain additional aboveground oil and gas facilities under different spatial resolutions in the Permian, Haynesville-Bossier, and Eagle Ford oil and gas basins. MethaneSAT oil and gas emissions estimates are spatially aggregated to coarser resolutions in this analysis, starting from a) the native MethaneSAT pixel resolution of 0.04° × 0.04°, then b) 0.25° × 0.25° which mimics the emissions inversion resolution of TROPOMI-based estimates for 2023 (*4*), c) 0.5° × 0.5° which matches the resolution of global oil/gas estimates using TROPMI data (*5*), and d) 1.0° × 1.0° which is the emissions inversion resolution of GOSAT-derived estimates of global methane emissions (*6*). e) Barplot displaying the total methane emissions from regions solely containing production well-pads across all four resolutions. As the resolution of the spatially-explicit methane emissions data coarsens, the quantity of data retained using this spatial filtering approach (i.e., areas solely containing production well-pads) drops, leading to decreased methane emissions.

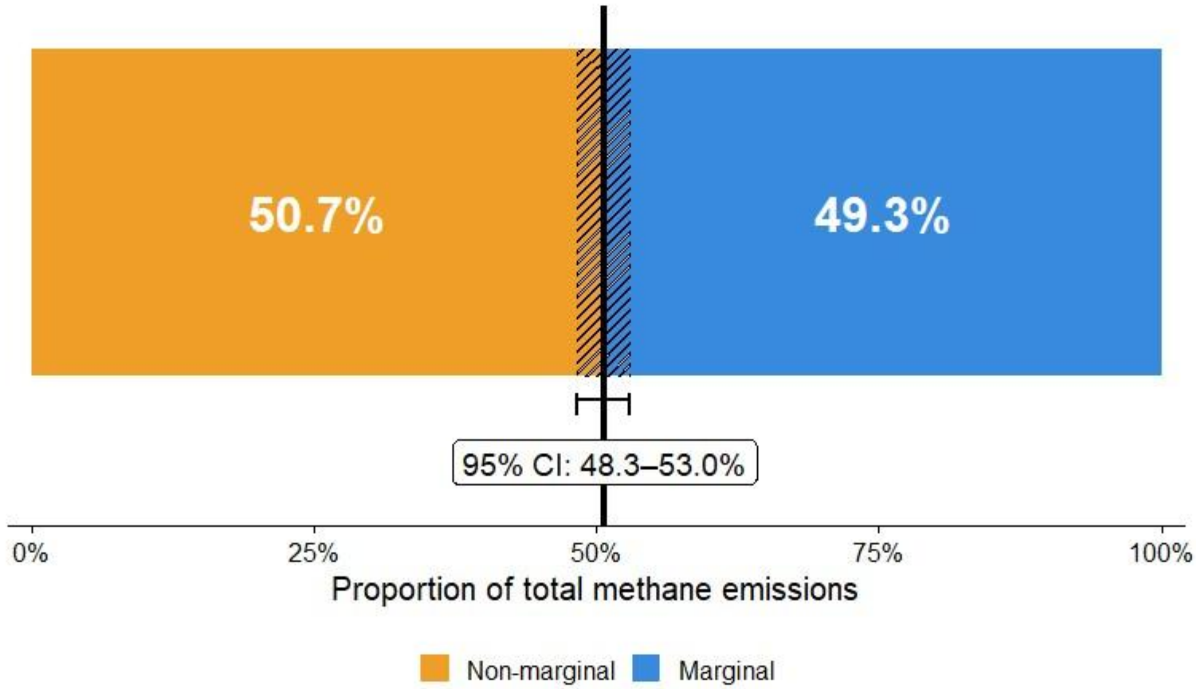


**Fig. S8.**
Results of a bootstrap resampling of grid cells with replacement (n=1,000) showing the relative methane emissions contributions from marginally (i.e., <15 boe $d^{-1}$ well-pad$^{-1}$) and non-marginally (i.e., ≥15 boe $d^{-1}$ well-pad$^{-1}$) producing areas.

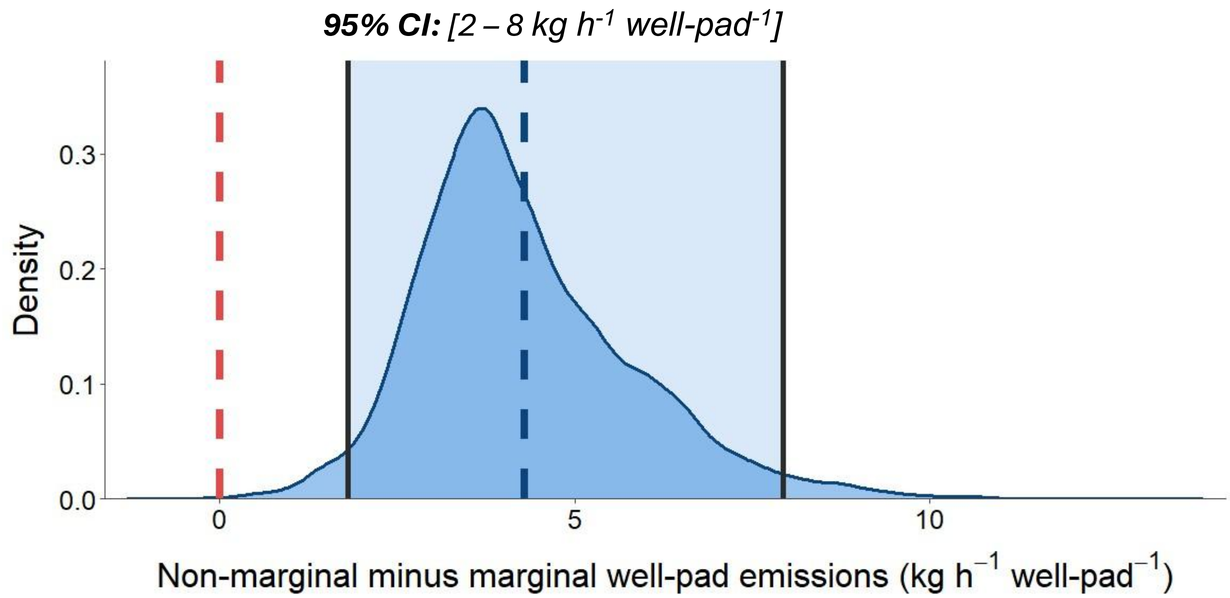


**Fig. S9.**

Results of a permutation test showing the difference in well-pad averaged methane emissions by grid cell from MethaneSAT estimates between non-marginally and marginally-producing grid cells. If the 95% confidence interval (i.e., black bars) overlaps 0 (i.e., red dashed line), this would indicate that the average well-pad normalized emissions between marginal and non-marginal grid cells are not statistically different. We draw 1,000 samples of well-normalized emissions (i.e., total production-related oil and gas emissions divided by the number of well-pads) from both marginally- and non-marginally producing grid cells and calculate the difference in means between the samples, which we repeat 10,000 times to produce the distribution shown above. Grid cells are defined as marginally- or non-marginally producing using the total production divided by the number of actively producing well-pads within the grid cell, with ≤15 boe $d^{-1}$ well-pad$^{-1}$ as the definition for a marginally-producing grid cell, and vice-versa.

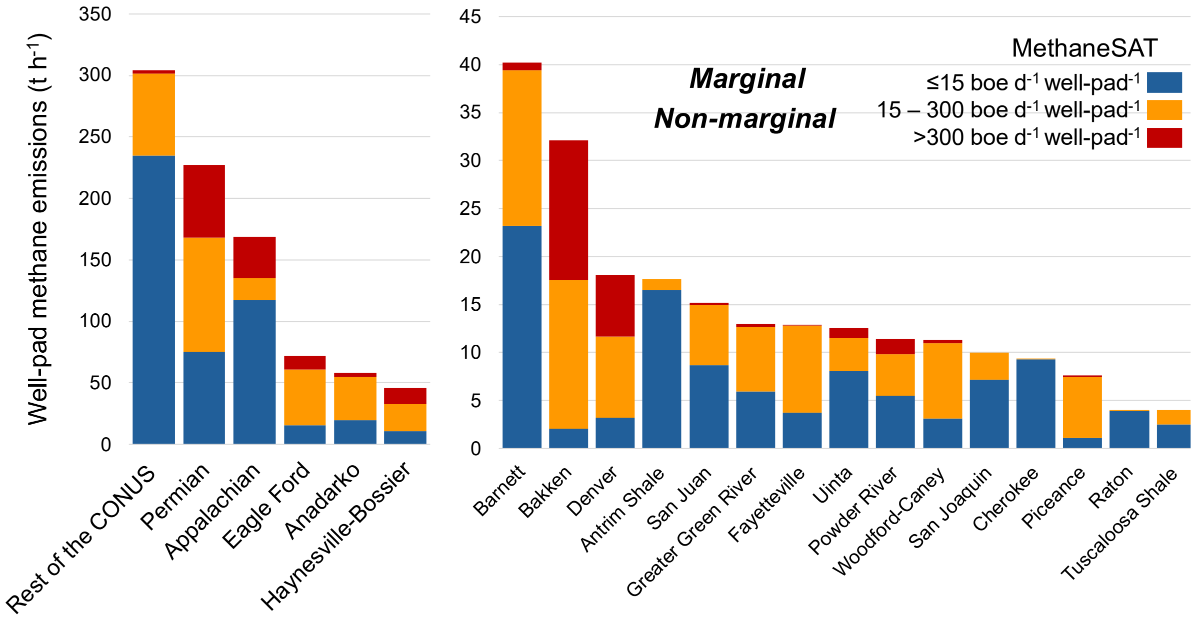


**Fig. S10.**

Grid-cell normalized well-pad emissions and breakdowns by production cohort for 20 major oil/gas producing basins in the U.S., including regions outside of the top 20 producing oil and gas basins (i.e., "Rest of the CONUS"). Grid-normalized production emissions are categorized as <15 boe $d^{-1}$ well-$pad^{-1}$, 15-300 boe $d^{-1}$ well-$pad^{-1}$, and >300 boe $d^{-1}$ well-$pad^{-1}$.

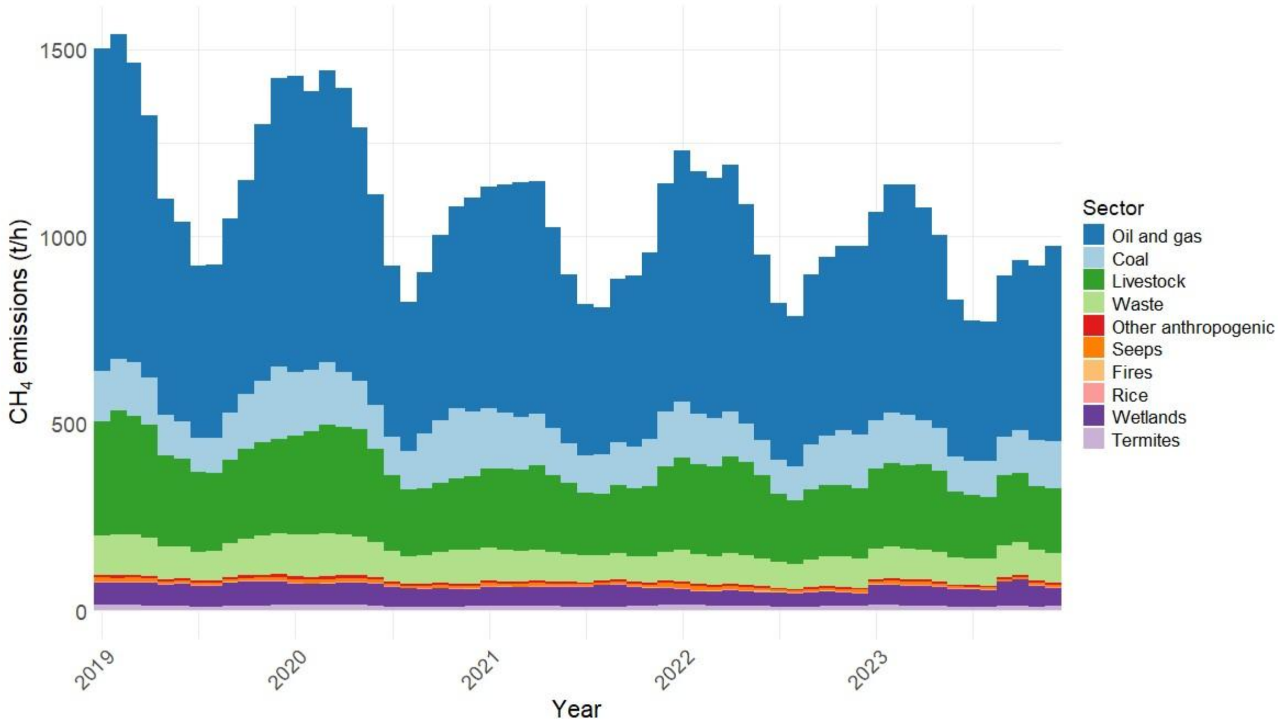


**Fig. S11.**

Monthly trends in sectoral methane emissions for 2019-2023 from gridded estimates derived from global TROPOMI observations using the localized ensemble transform Kalman filter (CHEEREIO v1.3.1) (*7*). Seasonal emissions from Pendergrass et al. (2025) are mapped at their native resolution of 200 × 250 km and calculated using an equal area weighting approach for the aggregated MethaneSAT spatial domains in the U.S.

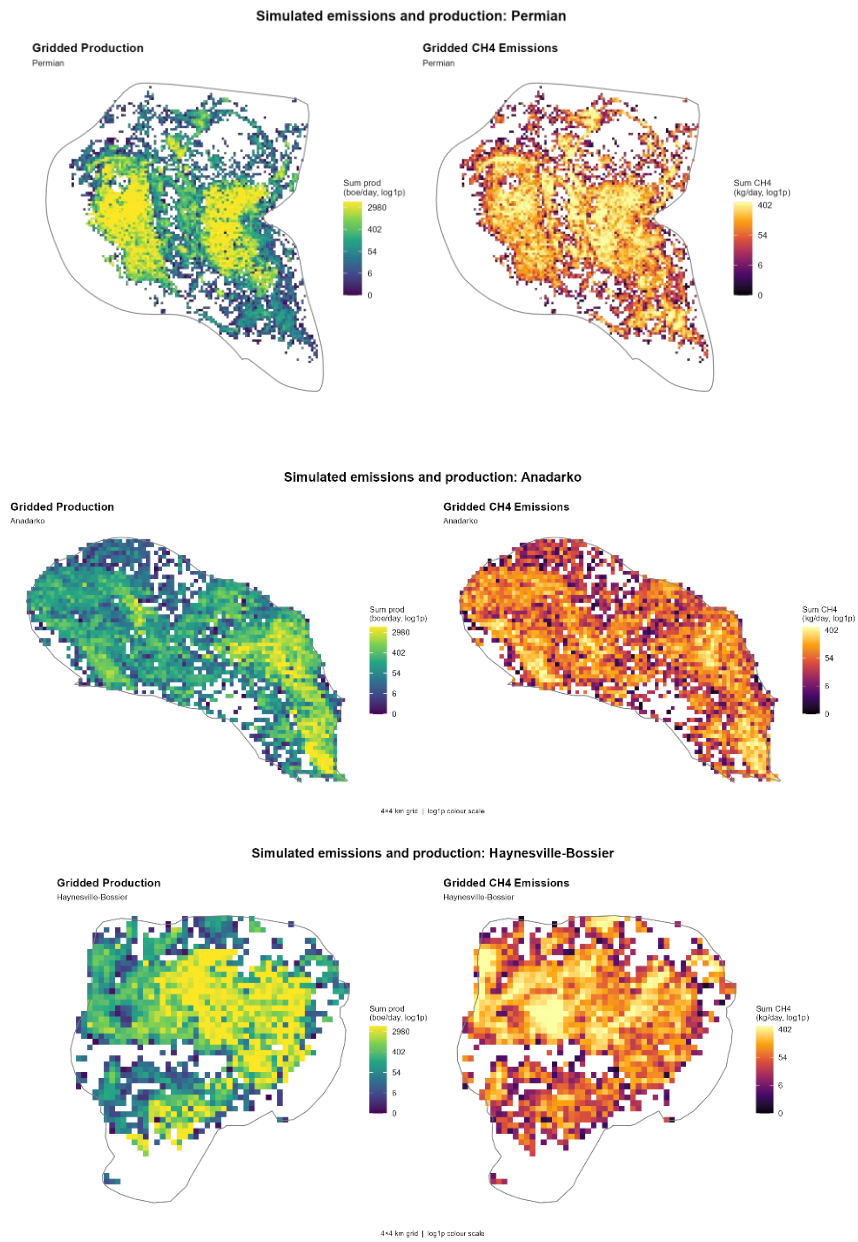


**Fig. S12.**

Examples of oil and gas production (left panels) and simulated methane emissions (right panels) gridded to the native MethaneSAT grid cell resolution of 4 × 4 km for the Permian basin (top), the Anadarko basin (middle), and the Haynesville-Bossie basin (bottom). Methane emissions are simulated at the well-pad level, which are then gridded to measure the differences between grid cell aggregated versus well-pad emissions by production cohort.

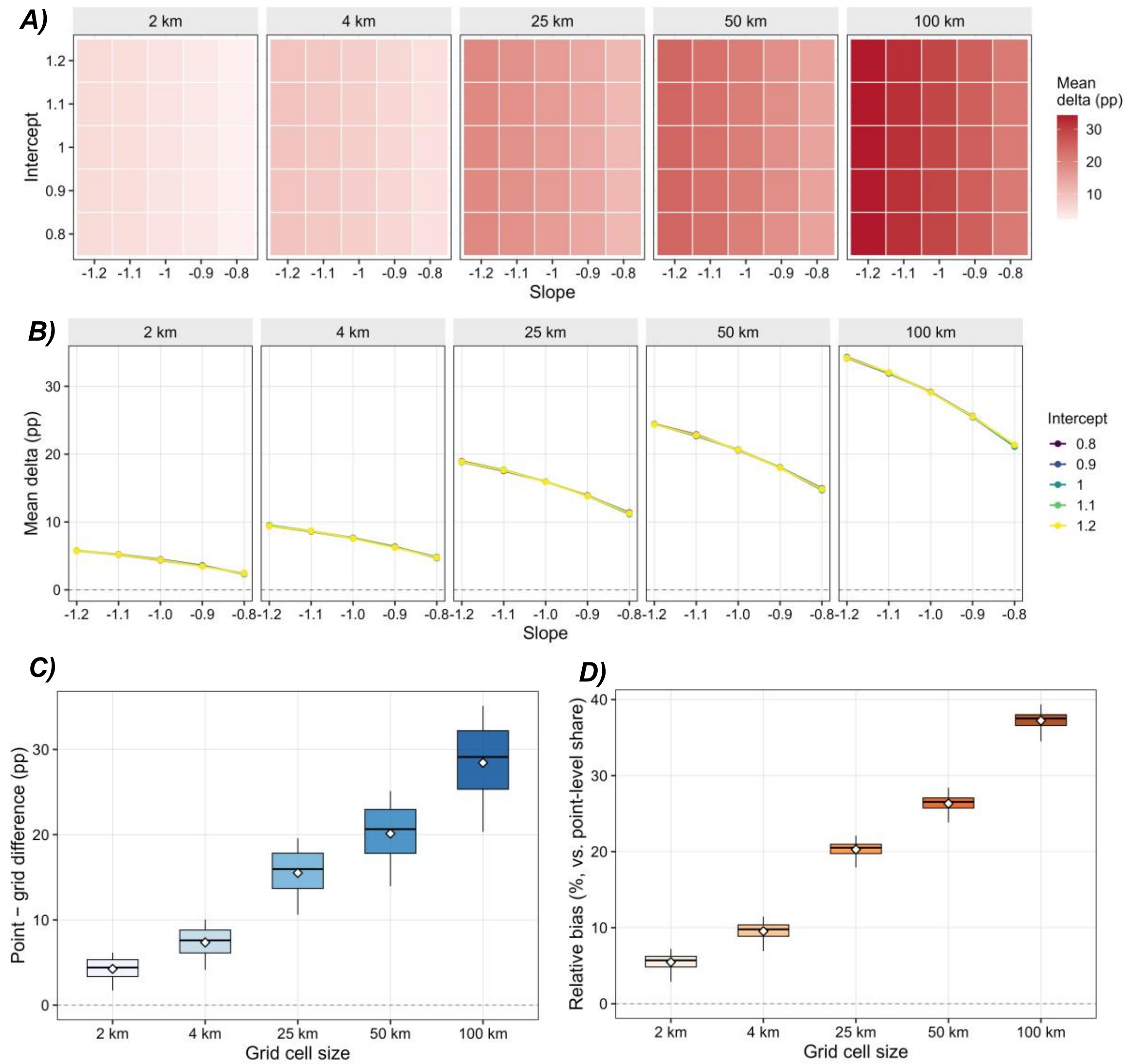


**Fig. S13.**

a) Heatmaps showing the mean difference in percentage points (i.e., mean delta) between the estimated proportion of emissions below 15 boe $d^{-1}$ well-pad$^{-1}$ for point (i.e., well-pad) and gridded production normalized by well-pad counts. The parameters of the intensity/production relationship are tested versus varying grid cell sizes. b) Trends in the mean delta values by varying the grid cell sizes, y-intercept, and slope values of the intensity/production relationship. c) Boxplots of the mean absolute difference in percentage points at varying grid cell sizes. d) Relative bias in the difference in percentage points between point- and gridded-production proportion of emissions. The relative biases are consistently higher for point-level proportions when compared to gridded production normalization, with the differences increasing with larger grid cells used in the production normalization.

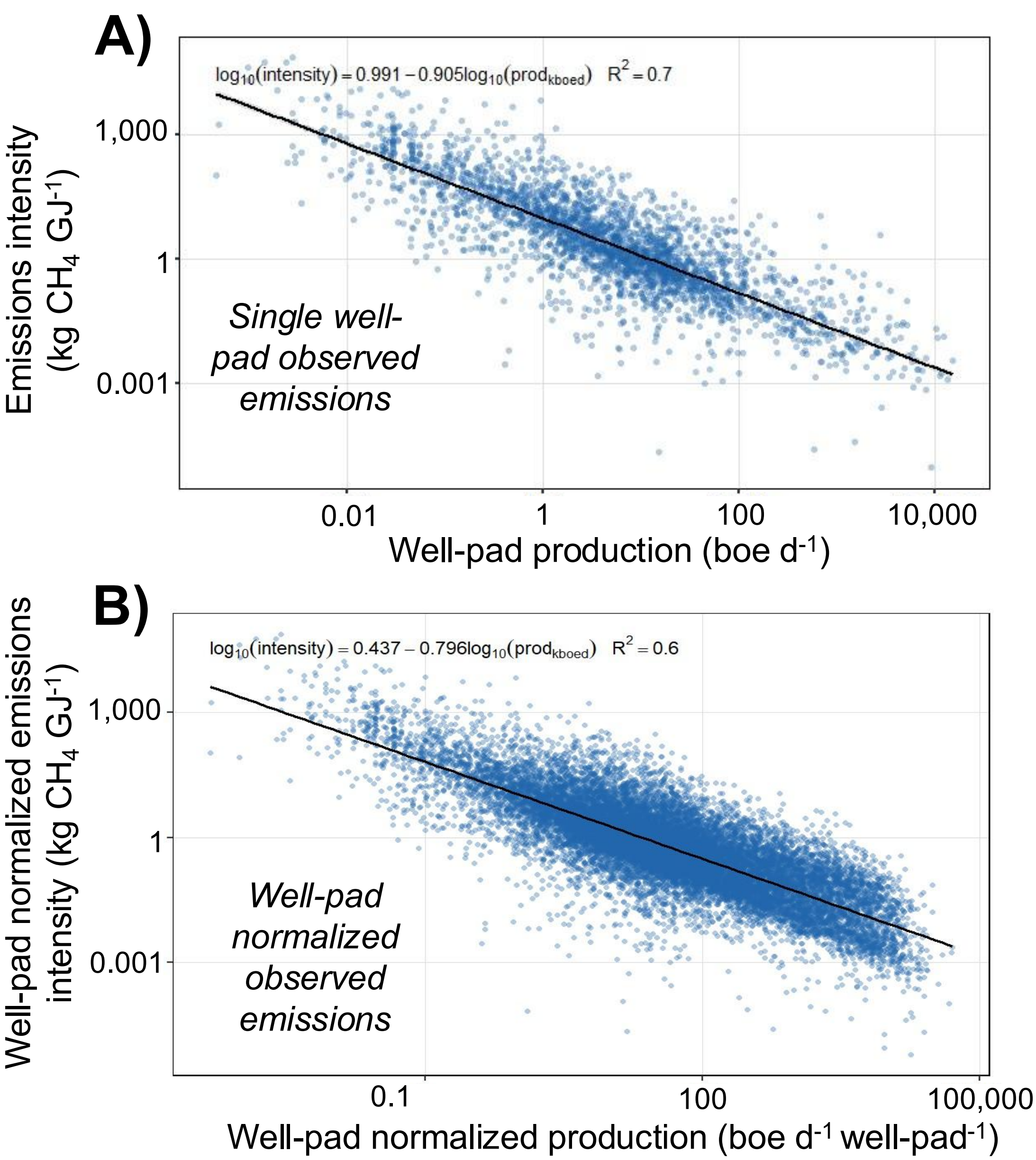


**Fig. S14.**

a) Relationship between energy intensity and oil and gas production for wells-only grid cells (i.e., 4 × 4 $km^2$) measured by MethaneSAT for grid cells containing a single well-pad, and b) for well-pad normalized energy intensity by normalized production from all observed wells-only grid-cells.

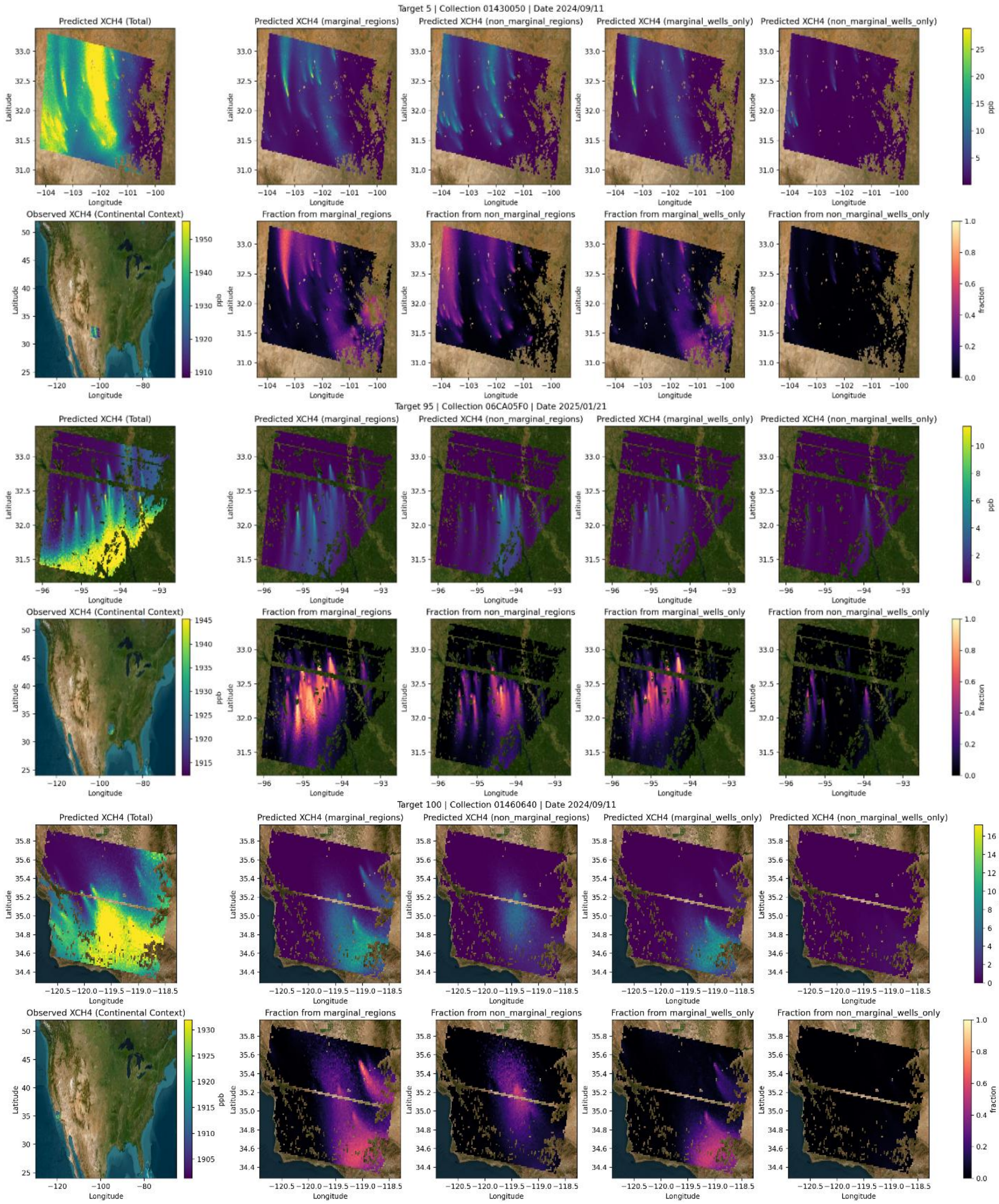


**Fig. S15.**

Sample maps of the posterior-predicted methane enhancements attributable to marginally producing regions, non-marginally producing regions, regions solely containing marginal well-pads, and those solely containing non-marginal well-pads from three MethaneSAT collections. The estimated contributions to the total methane enhancement, enabling identification of large emission sources with poorly distinguishable atmospheric signatures.

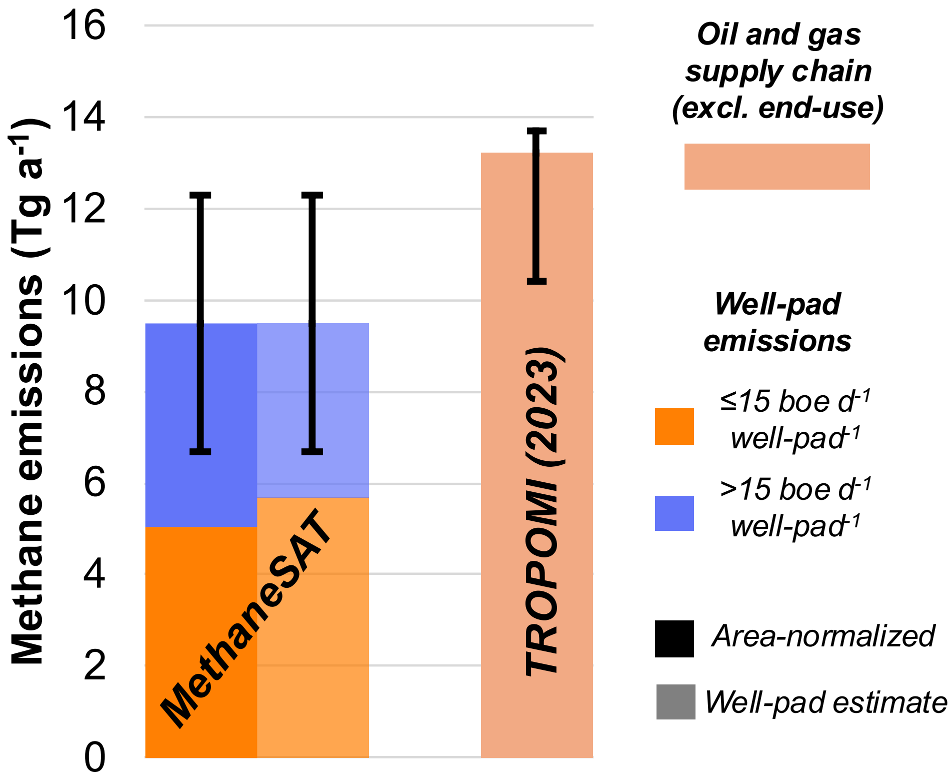


**Fig. S16.**

Comparison of area-normalized and actual well-pad emissions by production cohort from MethaneSAT emissions estimates for the CONUS. Actual well-pad emissions estimates by production cohort informed by MethaneSAT are based on the simulation results presented in the SI – Section 1. Well-pad emissions from MethaneSAT (left) are compared to total oil and gas emissions estimated by TROPOMI-based inversions for the CONUS for 2023 (right) (*4*) which correspond to total oil and gas supply chain methane emissions, excluding end-use sources like urban natural gas distribution meters.

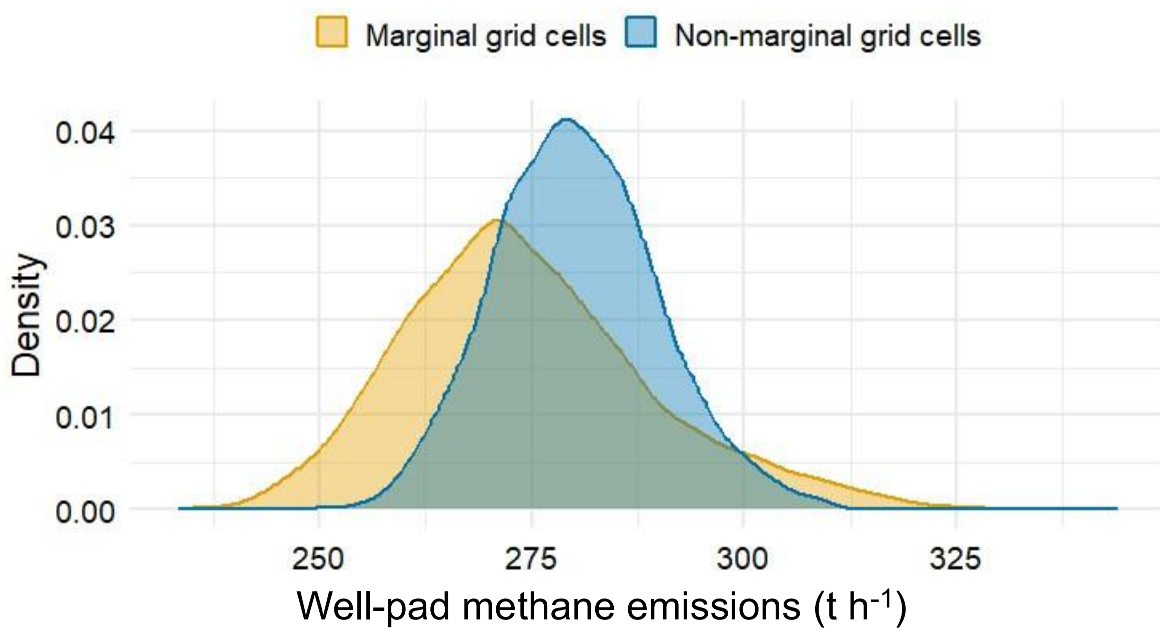


**Fig. S17.**

Normalized density plots of total methane emissions within marginally- and non-marginally-producing grid cells from MethaneSAT observations based on the 4,000 Hamiltonian Monte Carlo realizations contained within MethaneSAT observations.

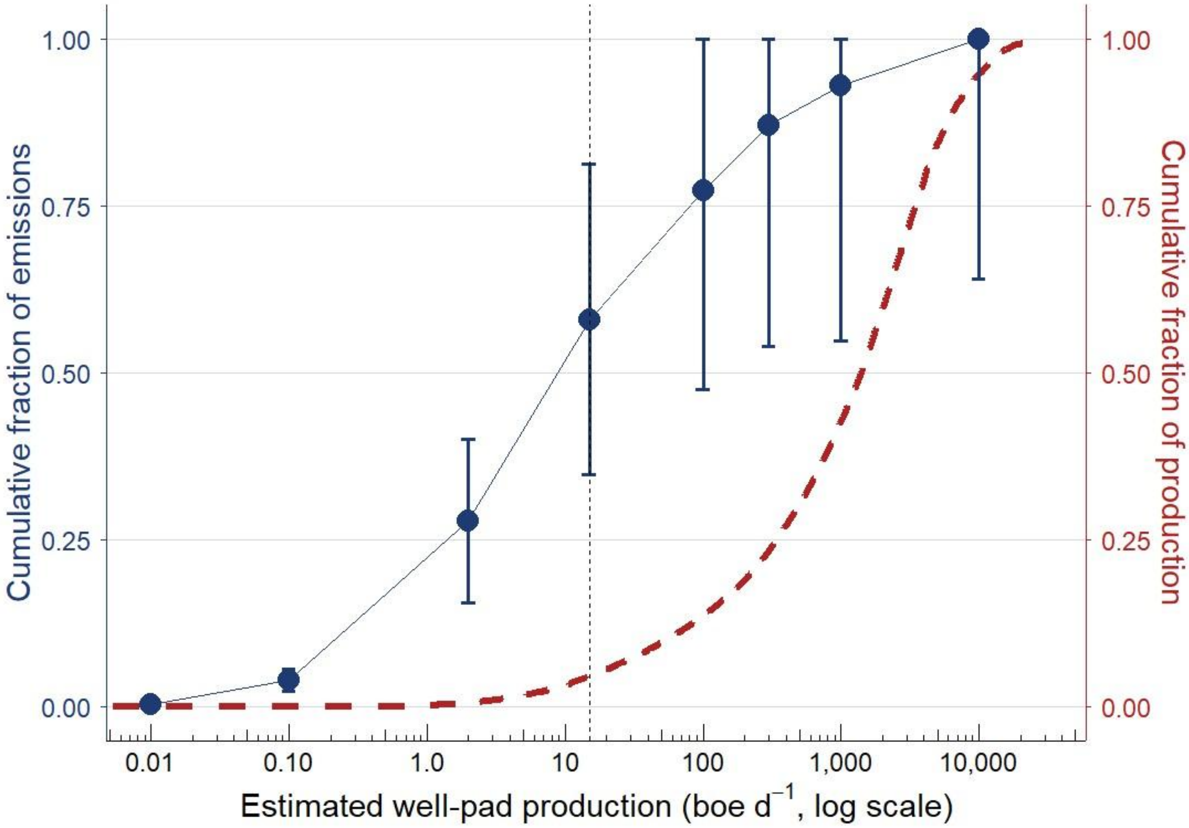


**Fig. S18.**

Cumulative methane emissions from estimated well-pad emissions and cumulative oil and gas production from well-pads within the CONUS. Estimated well-pad emissions proportions are calculated from simulations, with the methodological approach presented in the SI – Section 1.

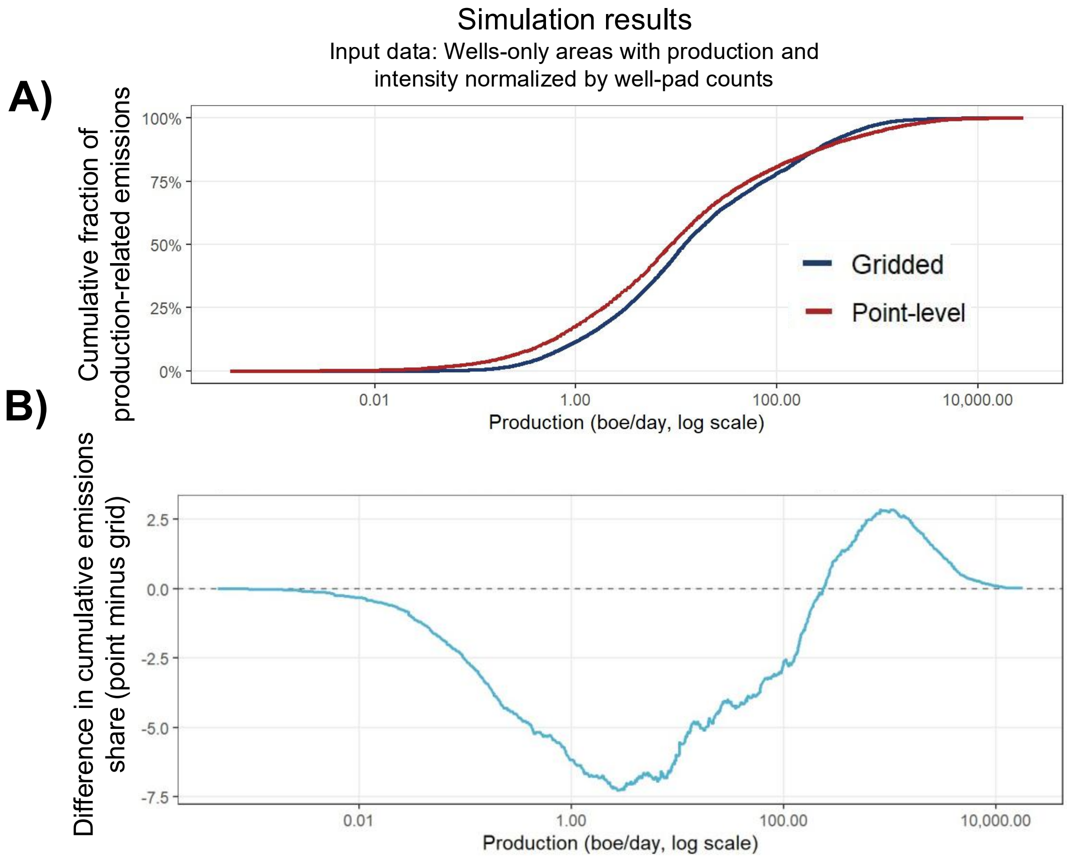


**Fig. S19.**

a) Cumulative emission curves by well-pad production from simulated point-level (i.e., well-pad) and gridded emissions data for the CONUS. Input data for the simulations is all wells-only areas with production and intensity normalized by well-pad counts. b) Differences in percentage points across production cohorts between gridded and point-level emissions proportions. Negative values indicate that point-level cumulative emissions are higher than grid-level at the respective production cohort, and vice-versa.

**Table S1.**

Description of 74 MethaneSAT scenes displaying retrieval data, associated region, and total methane emissions with uncertainty.

| BASIN | DATE | TARGET ID | PROCESSING ID | TOTAL EMISSIONS | LOWER BOUND | UPPER BOUND |
|---|---|---|---|---|---|---|
| **PERMIAN** | 09/11/2024 | 5 | 7869 | 235 | 175 | 298 |
| **PERMIAN** | 05/22/2024 | 6 | 7887 | 69 | 46 | 99 |
| **PERMIAN** | 06/14/2024 | 6 | 7886 | 132 | 91 | 181 |
| **PERMIAN** | 06/17/2024 | 56 | 8804 | 77 | 49 | 114 |
| **PERMIAN** | 09/16/2024 | 56 | 7860 | 30 | 16 | 49 |
| **PERMIAN** | 09/28/2024 | 56 | 7845 | 168 | 121 | 222 |
| **PERMIAN** | 09/29/2024 | 56 | 7843 | 140 | 101 | 185 |
| **PERMIAN** | 10/10/2024 | 56 | 7836 | 91 | 60 | 130 |
| **PERMIAN** | 10/12/2024 | 56 | 8804 | 77 | 49 | 114 |
| **PERMIAN** | 10/26/2024 | 56 | 7819 | 171 | 125 | 223 |
| **PERMIAN** | 11/22/2024 | 56 | 7791 | 201 | 150 | 259 |
| **PERMIAN** | 12/23/2024 | 56 | 7786 | 126 | 86 | 174 |
| **PERMIAN** | 03/20/2025 | 56 | 7752 | 117 | 86 | 153 |
| **PERMIAN** | 05/13/2025 | 56 | 8558 | 10 | 3 | 23 |
| **PERMIAN** | 09/30/2024 | 57 | 7842 | 175 | 131 | 225 |
| **PERMIAN** | 10/27/2024 | 57 | 7818 | 293 | 225 | 368 |
| **PERMIAN** | 12/26/2024 | 57 | 8722 | 34 | 15 | 64 |
| **PERMIAN** | 12/29/2024 | 57 | 7779 | 332 | 248 | 425 |
| **PERMIAN** | 03/19/2025 | 57 | 7755 | 169 | 118 | 233 |
| **PERMIAN** | 05/31/2025 | 57 | 7715 | 97 | 73 | 125 |
| **PERMIAN** | 03/21/2025 | 60 | 8618 | 96 | 62 | 138 |
| **PERMIAN** | 10/28/2024 | 61 | 7815 | 29 | 12 | 52 |
| **APPALACHIAN** | 09/05/2024 | 2 | 8890 | 159 | 119 | 206 |
| **APPALACHIAN** | 09/15/2024 | 2 | 8889 | 143 | 104 | 188 |
| **APPALACHIAN** | 10/12/2024 | 64 | 7834 | 44 | 24 | 79 |
| **APPALACHIAN** | 09/17/2024 | 67 | 7859 | 23 | 12 | 40 |
| **APPALACHIAN** | 09/28/2024 | 67 | 8886 | 140 | 84 | 212 |
| **APPALACHIAN** | 11/14/2024 | 67 | 7807 | 65 | 43 | 93 |
| **APPALACHIAN** | 02/20/2025 | 67 | 7766 | 18 | 7 | 35 |
| **APPALACHIAN** | 03/04/2025 | 68 | 8641 | 126 | 85 | 180 |
| **APPALACHIAN** | 04/30/2025 | 68 | 7739 | 79 | 55 | 107 |
| **EAGLE FORD** | 10/25/2024 | 85 | 7820 | 91 | 60 | 129 |
| **EAGLE FORD** | 11/22/2024 | 85 | 7790 | 85 | 62 | 112 |
| **EAGLE FORD** | 12/24/2024 | 85 | 7784 | 31 | 20 | 47 |
| **EAGLE FORD** | 12/25/2024 | 85 | 7783 | 67 | 44 | 94 |
| **EAGLE FORD** | 11/19/2024 | 90 | 7793 | 36 | 20 | 56 |
| **HAYNESVILLE** | 09/24/2024 | 95 | 8829 | 18 | 9 | 35 |
| **HAYNESVILLE** | 10/20/2024 | 95 | 7822 | 124 | 91 | 163 |
| **HAYNESVILLE** | 12/19/2024 | 95 | 8742 | 79 | 57 | 104 |
| **HAYNESVILLE** | 01/08/2025 | 95 | 8699 | 46 | 30 | 66 |

| | | | | | | |
|---|---|---|---|---|---|---|
| **HAYNESVILLE** | 01/21/2025 | 95 | 7767 | 122 | 81 | 173 |
| **HAYNESVILLE** | 02/24/2025 | 95 | 7762 | 80 | 59 | 104 |
| **HAYNESVILLE** | 03/31/2025 | 95 | 8601 | 49 | 31 | 71 |
| **SAN JOAQUIN** | 09/11/2024 | 100 | 7866 | 63 | 41 | 91 |
| **SAN JOAQUIN** | 10/20/2024 | 100 | 8973 | 42 | 26 | 64 |
| **SAN JOAQUIN** | 11/04/2024 | 100 | 7812 | 30 | 17 | 49 |
| **SAN JOAQUIN** | 11/21/2024 | 100 | 8963 | 38 | 26 | 52 |
| **SAN JOAQUIN** | 11/22/2024 | 100 | 8962 | 65 | 48 | 86 |
| **SAN JOAQUIN** | 05/08/2025 | 100 | 8915 | 42 | 30 | 56 |
| **SAN JOAQUIN** | 06/12/2025 | 100 | 8894 | 22 | 11 | 38 |
| **SAN JOAQUIN** | 09/12/2024 | 159 | 7864 | 78 | 56 | 105 |
| **SAN JOAQUIN** | 09/25/2024 | 159 | 7848 | 94 | 67 | 124 |
| **SAN JOAQUIN** | 05/09/2025 | 159 | 7733 | 146 | 109 | 189 |
| **SAN JUAN** | 11/15/2024 | 106 | 8885 | 26 | 12 | 46 |
| **POWDER RIVER** | 09/30/2024 | 115 | 7840 | 12 | 5 | 24 |
| **POWDER RIVER** | 10/28/2024 | 115 | 7814 | 5 | 2 | 10 |
| **POWDER RIVER** | 05/31/2025 | 115 | 7713 | 55 | 34 | 83 |
| **BAKKEN** | 10/12/2024 | 121 | 8803 | 8 | 3 | 20 |
| **BAKKEN** | 02/19/2025 | 121 | 8671 | 43 | 25 | 69 |
| **BAKKEN** | 05/13/2025 | 121 | 8557 | 7 | 2 | 16 |
| **BAKKEN** | 06/01/2025 | 121 | 8528 | 10 | 4 | 20 |
| **UINTA** | 07/21/2024 | 213 | 7881 | 11 | 6 | 21 |
| **UINTA** | 07/22/2024 | 213 | 7880 | 19 | 10 | 31 |
| **UINTA** | 09/09/2024 | 214 | 7872 | 3 | 1 | 11 |
| **GREATER GREEN RIVER** | 09/19/2024 | 217 | 8837 | 31 | 19 | 47 |
| **GREATER GREEN RIVER** | 09/20/2024 | 217 | 8887 | 4 | 1 | 10 |
| **GREATER GREEN RIVER** | 09/21/2024 | 217 | 7855 | 5 | 2 | 11 |
| **UINTA** | 10/02/2024 | 110 | 7839 | 15 | 7 | 29 |
| **UINTA** | 11/14/2024 | 110 | 7806 | 20 | 13 | 30 |
| **UINTA** | 01/20/2025 | 110 | 8882 | 11 | 6 | 20 |
| **UINTA** | 02/21/2025 | 110 | 8665 | 23 | 14 | 35 |
| **UINTA** | 02/24/2025 | 110 | 7763 | 30 | 18 | 46 |
| **UINTA** | 04/29/2025 | 110 | 7741 | 13 | 6 | 23 |
| **UINTA** | 05/02/2025 | 110 | 7738 | 16 | 10 | 24 |

**Table S2.**

Values associated with three factors tested within the well-pad simulations examining the differences between grid- and well-pad level production and emissions. Relative variable importance is also presented and was assessed using the permutation-based %IncMSE metric from the "randomForest" package in R (*8*). Values are unitless and used only for relative ranking of predictors within the simulation where higher values indicate a stronger impact on the overall analysis.

| Factor | Description | Values tested | Relative variable importance (%IncMSE) |
|---|---|---|---|
| Grid cell size | Grid cell size used to aggregate production and emissions data | $2 \times 2$ km$^2$, $4 \times 4$ km$^2$, $25 \times 25$ km$^2$, $50 \times 50$ km$^2$, $100 \times 100$ km$^2$ | 78 |
| Slope | Slope value in the intensity versus production relationship ($\log_{10}$ scale) used to estimate well-pad emissions for the simulations | -0.8, -0.9, -1.0, -1.1, -1.2 | 65 |
| Intercept | Y-intercept value in the intensity versus production relationship ($\log_{10}$ scale) used to estimate well-pad emissions for the simulations | 0.8, 0.9, 1.0, 1.1, 1.2 | -3 |

**Table S3.**

Comparison of area-normalized well-pad methane emissions for 2024 within the Permian basin from our MethaneSAT extrapolation to the CONUS and those estimated from an extensive Bridger LiDAR sampling campaign (*9*).

| Well-pad production cohort | MethaneSAT extrapolated emissions ($t\ h^{-1}$) | Proportion of emissions to total well-pads | Bridger extrapolated emissions ($t\ h^{-1}$) | Proportion of emissions to total well-pads |
|---|---|---|---|---|
| Marginal (<15 boe $d^{-1}$) | 75.1 | 33.1% | 82.0 | 35.4% |
| Standard (15 – 300 boe $d^{-1}$) | 92.9 | 40.9% | 109.0 | 47.1% |
| High producing (>300 boe $d^{-1}$) | 59.1 | 26.0% | 40.4 | 17.5% |
| Total | 227.2 | - | 231.5 | - |

**Table S4.**

Annual emission correction factors and adjusted oil and gas emissions based on monthly oil and gas emissions for 2023 from TROPOMI methane inversions using the localized ensemble transform Kalman filter CHEEREIO (*7*). All estimates are calculated for the full observation domains from MethaneSAT which can extend beyond the basin boundaries we use in this work.

| Observation region | Estimated oil and gas emissions ($t\ h^{-1}$) [95% CI] | Annual correction factor | Adjusted oil and gas emissions ($t\ h^{-1}$) [95% CI] |
|---|---|---|---|
| Appalachian | 137 [91 - 190] | 0.96 | 118 [80 - 161] |
| Bakken | 22 [11 - 36] | 1.00 | 22 [11 - 36] |
| Permian | 343 [249 - 435] | 1.04 | 329 [239 - 418] |
| Eagle Ford | 88 [59 - 117] | 1.25 | 110 [69 – 150] |
| Haynesville-Bossier | 77 [47 - 103] | 0.91 | 81 [52 – 110] |
| San Juan | 18 [7 - 34] | 0.61 | 11 [4 – 21] |
| San Joaquin | 22 [15 - 31] | 0.97 | 18 [12 – 27] |
| Powder River | 19 [9 - 29] | 1.28 | 38 [18 – 59] |
| Uinta/Piceance/Greater Green River | 26 [15 - 38] | 1.04 | 22 [11 – 35] |

**Table S5.**

Total marketed oil and gas production from Wood Mackenzie for 2024 for all of the oil and gas basins measured by MethaneSAT in this work based on total production within the basin extents and the fractions covered by MethaneSAT observations. A percentage coverage of >99% represents cases where MethaneSAT observations do not completely encompass all production within the basin boundaries.

| Observation region | Total marketed oil and gas production within the basin (kboe $d^{-1}$) | Total marketed oil and gas production covered within the basin (kboe $d^{-1}$) | Percentage of total basin production covered |
|---|---|---|---|
| Appalachian | 6,410 | 6,170 | 96% |
| Bakken | 1,840 | 1,830 | 99% |
| Permian | 10,890 | 10,890 | >99% |
| Eagle Ford | 2,380 | 2,380 | 100% |
| Haynesville-Bossier | 2,540 | 2,540 | >99% |
| San Juan | 370 | 370 | 100% |
| San Joaquin | 270 | 270 | >99% |
| Powder River | 350 | 320 | 91% |
| Uinta | 310 | 310 | >99% |
| Greater Green River | 480 | 270 | 56% |
| Piceance | 210 | 30 | 13% |

**Table S6. Description of well-pad infrastructure data within the entire CONUS.** Infrastructure breakdown of active production well-pads contained within marginally- and non-marginally producing grid cells normalized by total well-pad counts in the CONUS.

| | **Marginal grid cells (n = 35,791)** | **Non-marginal grid cells (n = 14,486)** |
|---|---|---|
| # total well-pads | 489,000 | 169,000 |
| # marginal well-pads | 467,000 | 77,900 |
| % marginal well-pads | 95% | 46% |
| # non-marginal well-pads | 22,300 | 90,900 |
| % non-marginal well-pads | 5% | 54% |
| Avg. count of marginal well-pads per grid cell | 13.0 | 5.4 |
| Avg. count of non-marginal well-pads per grid cell | 0.6 | 6.3 |
| % of total production within combined wells-only grid cells | 5% | 95% |
| Average production of marginal well-pads | 2.3 boe $d^{-1}$ well-pad$^{-1}$ | 4.7 boe $d^{-1}$ well-pad$^{-1}$ |
| Average production of non-marginal well-pads | 29 boe $d^{-1}$ well-pad$^{-1}$ | 320 boe $d^{-1}$ well-pad$^{-1}$ |

## References


1. C. A. Gotway, L. J. Young, Combining Incompatible Spatial Data. *Journal of the American Statistical Association* **97**, 632–648 (2002).

2. D. W. S. Wong, “The Modifiable Areal Unit Problem (MAUP)” in *WorldMinds: Geographical Perspectives on 100 Problems*, D. G. Janelle, B. Warf, K. Hansen, Eds. (Springer Netherlands, Dordrecht, 2004; http://link.springer.com/10.1007/978-1-4020-2352-1_93), pp. 571–575.

3. Wood Mackenzie (2021). https://www.woodmac.com/lens.

4. J. D. East, D. J. Jacob, D. Jervis, N. Balasus, L. A. Estrada, S. E. Hancock, M. P. Sulprizio, J. Thomas, X. Wang, Z. Chen, D. J. Varon, J. R. Worden, Worldwide inference of national methane emissions by inversion of satellite observations with UNFCCC prior estimates. *Nat Commun* **16**, 11004 (2025).

5. L. Shen, D. J. Jacob, R. Gautam, M. Omara, T. R. Scarpelli, A. Lorente, D. Zavala-Araiza, X. Lu, Z. Chen, J. Lin, National quantifications of methane emissions from fuel exploitation using high resolution inversions of satellite observations. *Nat Commun* **14**, 4948 (2023).

6. X. Lu, D. J. Jacob, Y. Zhang, J. D. Maasakkers, M. P. Sulprizio, L. Shen, Z. Qu, T. R. Scarpelli, H. Nesser, R. M. Yantosca, J. Sheng, A. Andrews, R. J. Parker, H. Boesch, A. A. Bloom, S. Ma, Global methane budget and trend, 2010–2017: complementarity of inverse analyses using in situ (GLOBALVIEWplus $CH_4$ ObsPack) and satellite (GOSAT) observations. *Atmospheric Chemistry and Physics* **21**, 4637–4657 (2021).

7. D. C. Pendergrass, D. J. Jacob, N. Balasus, L. Estrada, D. J. Varon, J. D. East, M. He, T. A. Mooring, E. Penn, H. Nesser, J. R. Worden, Trends and seasonality of 2019–2023 global methane emissions inferred from a localized ensemble transform Kalman filter (CHEEREIO v1.3.1) applied to TROPOMI satellite observations. *Atmospheric Chemistry and Physics* **25**, 14353–14369 (2025).

8. A. Liaw, M. Wiener, Classification and regression by randomForest. *R news* **2**, 18–22 (2002).

9. C. P. Donahue, K. Oberoi, J. W. Dillon, V. Hengst, B. Kennedy, W. Kearney, J. Lennox, E. Rehbein, R. Sykes, C. D. Dudiak, D. T. Altamura, G. Doherty, P. A. Roos, J. K. Brasseur, M. J. Thorpe, Aerial LiDAR-Based, Source-Resolved Methane Emissions Inventory: Permian Basin Case Study for Benchmarking U.S. Emissions. *Environ. Sci. Technol.* **60**, 13968–13979 (2026).